MOUNTAIN-PLAINS CONSORTIUM

MPC 24-522 | M. Shakouri, C. Zhang and K. Ksaibati

BENEFICIAL REUSE OF LANDFILLED FLY ASH IN TRANSPORTATION INFRASTRUCTURE

A University Transportation Center sponsored by the U.S. Department of Transportation serving the Mountain-Plains Region. Consortium members:

Colorado State University
North Dakota State University
South Dakota State University
University of Colorado Denver
University of Denver
University of Utah
Utah State University
University of Wyoming

Technical Report Documentation Page

1. Report No.
MPC-683

2. Government Accession No.

3. Recipient's Catalog No.

4. Title and Subtitle
Beneficial Reuse of Landfilled Fly Ash in Transportation Infrastructure

5. Report Date
May 2024

6. Performing Organization Code

7. Author(s)
Mahmoud Shakouri, PhD
Chengyi Zhang, PhD
Khaled Ksaibati, PhD

8. Performing Organization Report No.
MPC 24-522

9. Performing Organization Name and Address
Colorado State University
1584 Campus Delivery
Fort Collins, Colorado 80523

10. Work Unit No. (TRAIS)

11. Contract or Grant No.

12. Sponsoring Agency Name and Address
Mountain-Plains Consortium
North Dakota State University
PO Box 6050, Fargo, ND 58108

13. Type of Report and Period Covered
Final Report

14. Sponsoring Agency Code

15. Supplementary Notes
Supported by a grant from the US DOT, University Transportation Centers Program

16. Abstract

This research explores the influence of thermo-mechanical beneficiation methods on the physicochemical characteristics and reactivity of fly ashes disposed of in landfills (LFAs) obtained from power plants in Wyoming and Colorado, USA. An in-depth assessment was conducted on the mechanical and performance aspects of mortar samples incorporating these LFAs, including reactivity, compressive strength, electrical resistivity, resistance to alkali-silica reaction-induced expansion, water absorption, and chloride permeation. The findings indicate that the beneficiation processes effectively enhanced the properties of the substandard ashes, ensuring that all beneficiated ashes met the rigorous standards set by ASTM C618. Thermo-mechanical beneficiation notably improved the physicochemical properties of LFAs, resulting in a reduction in loss on ignition (LOI) and an increase in fineness. The results demonstrated enhancements in the strength activity index of all LFAs post-beneficiation, surpassing the minimum requirement of 75% at 28 days. Furthermore, beneficiation increased heat release and calcium hydroxide consumption, indicating improved pozzolanic reactivity. In most instances, the mortar samples exhibited comparable or superior mechanical and durability performance compared with ASTM C618-compliant fly ash. These findings underscore the potential of beneficiated and reclaimed LFAs as practical alternatives in concrete production, particularly in light of the expected shortage of fly ash in the U.S. and globally.

17. Key Word
admixtures, fly ash, recycled materials

18. Distribution Statement
Public distribution

19. Security Classif. (of this report)
Unclassified

20. Security Classif. (of this page)
Unclassified

21. No. of Pages
65

22. Price
n/a

Form DOT F 1700.7 (8-72) Reproduction of completed page authorized

Beneficial Reuse of Landfilled Fly Ash in Transportation Infrastructure

Mahmoud Shakouri, Ph.D. [1]
Chengyi Zhang, Ph.D. [3]
Khaled Ksaibati, Ph.D. [3,4]

[1] Department of Construction Management, Colorado State University, Fort Collins, CO 80523
[3] Department of Civil and Architectural Engineering and Construction Management
University of Wyoming, Laramie, WY 802071
[4] Wyoming Technology Transfer Center, University of Wyoming, Laramie, WY 802071

May 2024

Acknowledgments

This project is funded by Mountain-Plains Consortium (MPC) under grant number MPC-683. The opinions and findings of the authors do not necessarily reflect the view and opinions of MPC.

Disclaimer

ABSTRACT[1]

This research explores the influence of thermo-mechanical beneficiation methods on the physicochemical characteristics and reactivity of fly ashes disposed of in landfills (LFAs) obtained from power plants in Wyoming and Colorado, USA. An in-depth assessment was conducted on the mechanical and performance aspects of mortar samples incorporating these LFAs, including reactivity, compressive strength, electrical resistivity, resistance to alkali-silica reaction-induced expansion, water absorption, and chloride permeation. The findings indicate that the beneficiation processes effectively enhanced the properties of the substandard ashes, ensuring that all beneficiated ashes met the rigorous standards set by ASTM C618. Thermo-mechanical beneficiation notably improved the physicochemical properties of LFAs, resulting in a reduction in loss on ignition (LOI) and an increase in fineness. The results demonstrated enhancements in the strength activity index of all LFAs post-beneficiation, surpassing the minimum requirement of 75% at 28 days. Furthermore, beneficiation increased heat release and calcium hydroxide consumption, indicating improved pozzolanic reactivity. In most instances, the mortar samples exhibited comparable or superior mechanical and durability performance compared with ASTM C618-compliant fly ash. These findings underscore the potential of beneficiated and reclaimed LFAs as practical alternatives in concrete production, particularly in light of the expected shortage of fly ash in the U.S. and globally.

---

[1] This report is based on the contents from the following published journal papers:
Shakouri, M., Teymouri, M., Vaddey, N. P., Zhang, C., Ksaibati, K., Kuinkel, M. S., & Liu, P. (2023). “Enhancing physiochemical properties and reactivity of landfilled fly ash through thermo-mechanical beneficiation.” *Cement and Concrete Composites*, 144, 105310.
Shakouri, M., Ahmed, A. A., & Teymouri, M. (2024). “Evaluating the performance of thermomechanically beneficiated fly ash blended mortar.” *Construction and Building Materials*, 411, 134401.

TABLE OF CONTENTS

LIST OF TABLES

LIST OF FIGURES

EXECUTIVE SUMMARY

This research seeks to assess the effectiveness of thermomechanically beneficiated landfilled fly ashes (LFA) obtained from landfills in Wyoming and Colorado, USA, as a viable substitute for traditional fly ash in the production of concrete.

Background

In the concrete industry, supplementary cementitious materials (SCMs) are vital for their contributions to enhanced mechanical performance, increased durability, reduced energy consumption, and decreased greenhouse gas emissions. Fly ash, a notable SCM derived from coal combustion in power plants, improves concrete workability, strengthens later age performance, and enhances resistance against various forms of deterioration. However, traditional fly ash in North America has experienced significant shifts in availability and quality over the past decade. Strict air pollution regulations targeting coal-fired power plants have impacted the operation and control of these facilities, altering the composition and characteristics of generated fly ash. Additionally, the shift in the energy production landscape toward natural gas has led to a decrease in fly ash production, affecting its suitability for concrete use. These interconnected challenges necessitate a reevaluation of conventional fly ash supply, urging the exploration of alternative solutions to ensure a consistent and suitable supplementary cementitious material for the concrete industry.

Traditionally, unused fly ash has been managed through landfilling and surface impoundments due to storage limitations in power plants. In this context, a considerable portion of fly ashes designated for landfills is often labeled as “off-spec,” indicating non-compliance with standards regulating the use of coal fly ash in U.S. concrete mixtures. Nonetheless, there is substantial potential to reclaim LFAs and repurpose them following beneficiation. This is in line with the ongoing movement to reduce the carbon footprint associated with the cement and concrete industry.

Methodology

Landfilled fly ash was sampled from the Jim Bridger and Dave Johnson power plants in Wyoming and Nucla station in Colorado. The chemical and physical properties of these LFAs in the as-received condition were evaluated, and those not conforming to ASTM C618 requirements underwent mechanical and thermal beneficiation, involving grinding in a ball mill and exposure to high temperatures in a muffle furnace. A comprehensive set of experiments was conducted to assess the performance of mortars that combine ordinary Portland cement (OPC) and beneficiated LFA in terms of physical and chemical properties, reactivity, compressive strength, electrical resistivity, resistance to alkali-silica reaction-induced expansion, water absorption, and chloride permeation.

Results

This study’s findings show that thermo-mechanical beneficiation significantly impacts the physiochemical properties of landfilled fly ashes, resulting in reduced carbon content and increased fineness. X-ray diffraction analysis showed minimal changes in mineral composition post-beneficiation. LFAs, especially after beneficiation, exhibited improved reactivity as indicated by the strength activity index and modified R^3 tests. Higher temperatures led to a notable reduction in LOI, with implications for enhancing fly ash reactivity. Beneficiated LFAs performed well, achieving strength levels comparable to or exceeding OPC and ASTM compliant fly ash. LFAs exhibited evolving electrical resistivity, surpassing OPC after 56 days, suggesting microstructural improvements. LFAs, particularly the sample from Nucla station, demonstrated greater resistivity than FA, indicating improved microstructure. LFAs

show reduced chloride ingress, with UNucla surpassing ASTM compliant fly ash, highlighting enhanced resistance. LFAs effectively suppressed ASR-induced expansion and reduced water absorption rates, indicating enhanced durability potential and improved water penetration resistance.

1. INTRODUCTION

Supplementary cementitious materials (SCMs) play a crucial role in the concrete industry, offering advantages like enhanced mechanical performance, increased durability, reduced energy consumption, and diminished greenhouse gas emissions [1-5]. One notable material in this category is fly ash, a by-product of coal combustion in power plants, which brings about various benefits. It improves the workability of concrete, augments later age strength, and fortifies concrete durability against diverse forms of deterioration [6-9]. These positive outcomes arise from the pozzolanic reaction between fly ash and Portland cement, leading to the production of additional calcium silicate hydrate (C-S-H), decreased porosity, and increased mass transport resistance in concrete [10-13].

Nevertheless, the availability and quality of traditional fly ash have undergone significant shifts over the past decade in North America [14, 15]. Stringent air pollution regulations targeting emissions from coal-fired power plants have resulted in modifications to the operation and control of these facilities, impacting the composition and characteristics of the generated fly ash [16]. Furthermore, a noticeable transition in the energy production landscape—moving away from coal-fired power plants toward alternative sources like natural gas—has caused a reduction in fly ash production, diminishing its availability and affecting its suitability for use in concrete [17, 18]. These intertwined factors mandate a reevaluation of the conventional fly ash supply, prompting the exploration of alternative solutions to ensure a consistent and suitable supplementary cementitious material for the concrete industry [19-22].

Traditionally, unutilized fly ash has been handled through landfilling and surface impoundments, primarily due to storage limitations in power plants [23-25]. According to a recent report by the American Coal Ash Association (ACAA), approximately 28 million tons of fly ash were generated in the U.S. in 2021 [26]. Out of this total, roughly 11.9 million tons found application in concrete, while around 9.2 million tons were disposed of in landfills. A substantial proportion of fly ashes discarded in landfills (LFAs) is often categorized as “off-spec,” indicating their non-compliance with ASTM C618 [26] or AASHTO M295 [27] standards that regulate coal fly ash usage in U.S. concrete mixtures. These off-spec ashes frequently manifest characteristics like inadequate fineness or elevated loss on ignition (LOI), leading to their exclusion from ASTM C618 [26] or AASHTO M 295 [27] specifications due to the failure to meet stipulated requirements. As a result, the incorporation of landfilled fly ash in concrete production has been constrained. Notably, based on historical trends in coal fly ash generation and disposal, an estimated quantity of nearly 5 billion tons of coal fly ash has been deposited in landfills proximate to U.S. power plants [28]. Moreover, the global annual escalation in coal fly ash deposition is approximately 0.5 billion tons [29]. This accumulation signifies a substantial opportunity to extract and process these ashes, aiming to enhance their quality and render them more suitable for use in concrete [30].

For many years, a specific standard for assessing the compliance of collected LFAs has been lacking. Consequently, researchers and practitioners have adhered to the chemical and physical criteria outlined in the ASTM C618 standard [31]. In March 2023, a revised version of ASTM C618 was introduced [26], broadening the definition of coal ash to encompass harvested ash from landfills and impoundments, along with bottom ash. Notably, there were no alterations to the chemical and physical requirements, and LFAs are still expected to meet the previous specifications.

The utilization of an LFA often presents challenges due to its elevated carbon content, particle agglomeration, partial hydration, and reduced reactivity. Various approaches can be employed to tackle these challenges [32]. A cost-effective method involves leveraging the distinction in particle size distribution between carbon particles and LFA through dry sieving. McCarthy et al. [33] demonstrated the effectiveness of sieving LFA through a 63-µm sieve, resulting in a significant reduction in LOI from 6.1% to 3.2%. Another method, liquid-suspension gravity separation, combines fly ash with a liquid, typically water, relying on the differing densities and settling behaviors of fine and coarse particles in fly ash to segregate various particle sizes [34, 35]. However, this technique is mainly applied in laboratory settings for isolating and subsequently analyzing carbon particles [17-19]. Additional separation techniques, such as ultrasonic sieving and electrostatic separation, have been employed to decrease the LOI of ash [36-38]. Notably, electrostatic separation methods have found commercial application in separating unburned carbon from fly ash.

Less common techniques for carbon separation have been explored in the literature, including methods like chemical passivation, fluidization, and acid digestion [39]. In the chemical passivation process, a sacrificial surfactant is introduced into the fly ash, binding to carbon particle surfaces and preventing their absorption of air-entraining admixtures in concrete. It is crucial to highlight that this approach does not diminish the LOI value; rather, it serves to neutralize carbon. Fluidization entails introducing a non-reactive gas, such as helium, into a vertical tube containing a small sample, causing ash particles to ascend to the upper portion of the tube [40, 41]. Finally, acid digestion involves removing mineral components from fly ash through exposure to acids like hydrofluoric and hydrochloric acids, resulting in the exclusive retention of carbon particles [42].

Heat treatment represents another strategy to diminish the carbon content and LOI. The process of burning off excess carbon in LFAs typically requires temperatures ranging from 400°C to 800°C [43]. However, if the LFA contains heavy metal contaminants, higher temperatures exceeding 1,200°C may be necessary [44]. Such elevated temperatures can significantly escalate costs and potentially compromise the environmental advantages associated with LFA usage. Hence, a thorough consideration of the cost-benefit analysis of thermally beneficiating LFA is essential. Mechanical grinding of LFA is yet another approach employed to enhance its pozzolanic reactivity. By breaking down the LFA’s porous particles, the surface area is increased, which positively correlates with improved reactivity [45, 46].

Recent investigations into landfilled fly ash have delved into various facets, such as the utilization of high-sulfur and high-alkali fly ash sourced from coal-fueled power plants equipped with desulfurization systems [23]. Research studies have explored the recovery of fly ash from wet-storage areas for concrete applications [33], delved into the pozzolanic properties of fluidized bed combustion fly ash [21], and even assessed the use of unmanned aerial vehicles (UAVs) for estimating fly ash quantities in landfills [47]. Given the inherent diversity of properties within LFAs, compounded by the influence of assorted contaminants and environmental conditions on their characteristics, proposing a universal solution to enhance LFA performance becomes a formidable challenge. Therefore, it is imperative to investigate each LFA source independently to garner reliable and accurate results.

In light of the anticipated scarcity in fly ash supply, this study aims to evaluate the performance of thermomechanically beneficiated LFA sourced from landfills in Wyoming and Colorado, USA, as a potential alternative to conventional fly ash in concrete production. The distinctive aspect of this research lies in its thorough exploration of source-specific variables and the application of thermomechanical beneficiation techniques. The study employs a comprehensive series of experiments to assess the performance of mortars blending ordinary Portland cement (OPC) and LFA, considering various critical parameters. These parameters encompass physical and chemical properties, reactivity, compressive strength, electrical resistivity, resistance to alkali-silica reaction-induced expansion, water absorption, and chloride permeation. Collectively, these evaluations serve as crucial benchmarks for gauging the material’s long-term durability and its ability to withstand real-world challenges related to deterioration and durability.

2. LANDFILLED FLY ASH SAMPLE COLLECTION

2.1 Power Plants

2.1.1 Jim Bridger Power Plant

The Jim Bridger Power Plant is a 2,441.9 MW coal-fired power station operated by PacifiCorp near Point of Rocks, Wyoming. Established in 1974, the power plant is located southwest of Wyoming, as shown in Figure 2.1. There are four 565 MW power generation units currently in operation. Of these four units, two are in the process of being converted into gas. The plant currently has one industrial landfill and two flue gas desulphurization (FGD) ponds in operation and the construction of an additional FGD pond is forthcoming.

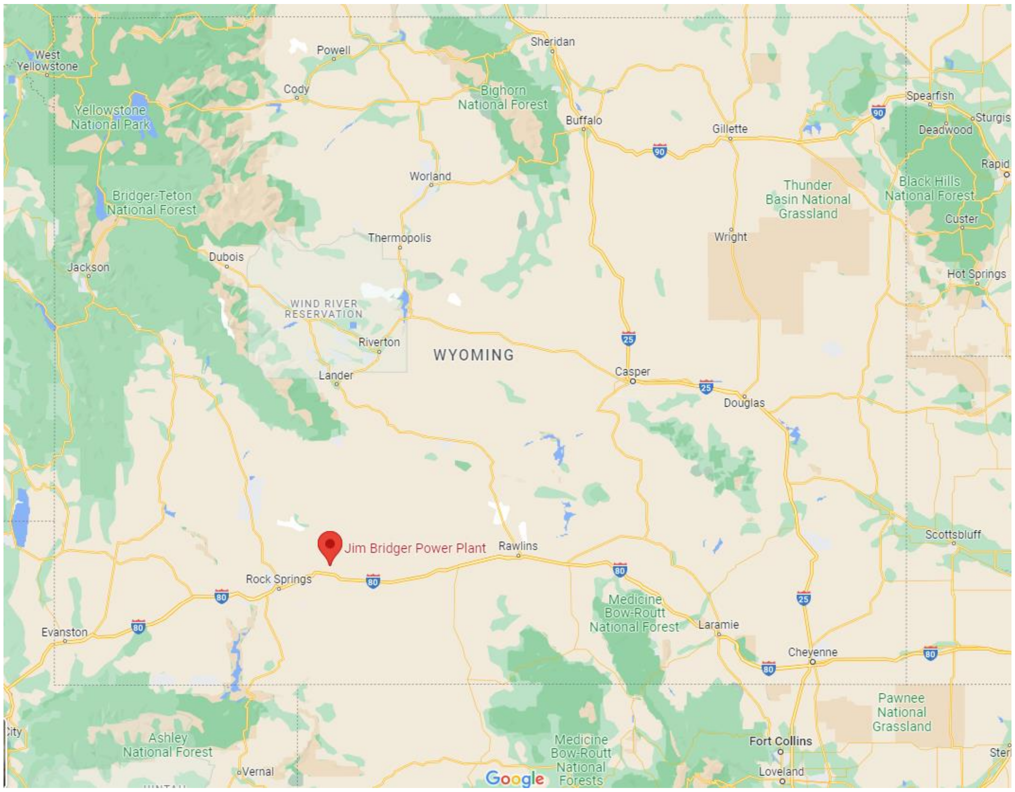

Figure 2.1 Location map of Jim Bridger Power Plant

2.1.1.1 Industrial Landfill at Jim Bridger Power Plant

The industrial landfill is in a long shallow valley approximately three miles north of the plant, as shown in Figure 2.2. The landfill is used for the disposal of dry bottom ash, fly ash, and industrial solid waste. Construction of the landfill began in the spring of 1986 and started to receive ash in July 1986. The total landfill area comprises approximately 234 acres of land. The only source of incoming waste to the landfill is the plant. No waste materials from the public are accepted for disposal.

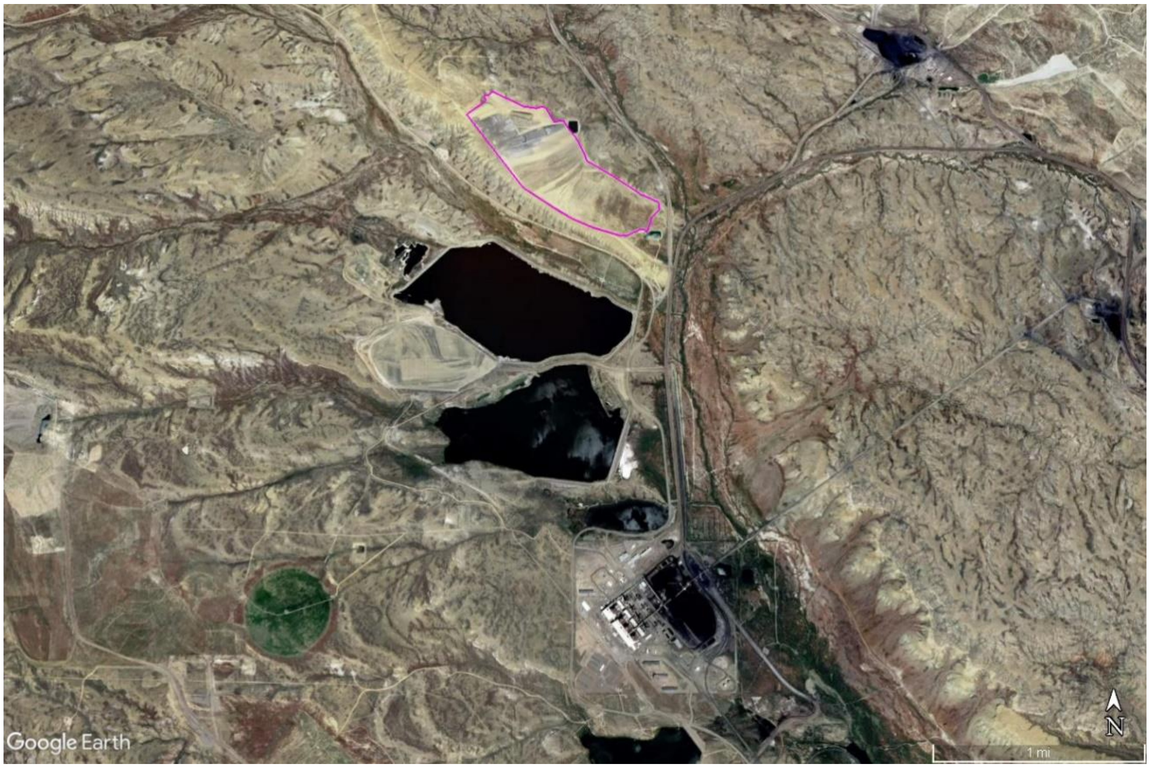

Figure 2.2 Industrial landfill at Jim Bridger Power Plant

2.1.2 Dave Johnston Power Plant

The Dave Johnston Power Plant is a 922.2 MW coal-fired power station operated by PacifiCorp near Glenrock, Wyoming. Established in 1959, the power plant lies in the central east of Wyoming, as shown in Figure 2.3. Four power generation units are currently in operation: Unit 1: 133.6 MW, Unit 2: 133.6 MW, Unit 3: 255.0 MW, and Unit 4: 400.0 MW. The plant currently has two CCR units: expansion landfill and ash pond.

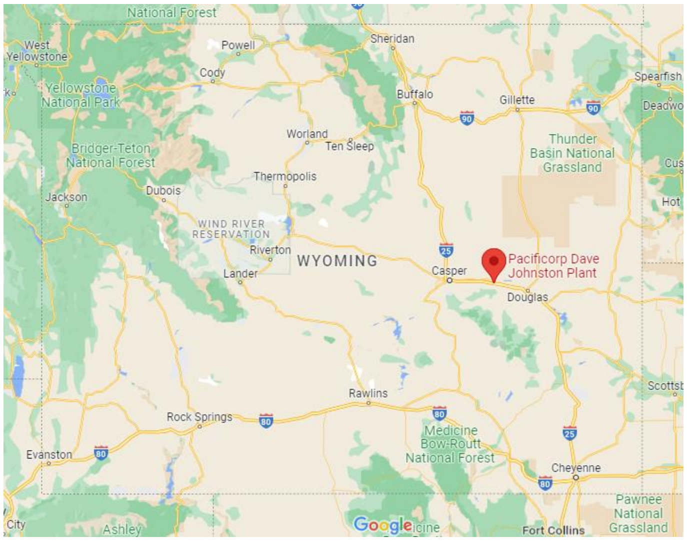

Figure 2.3 Location map of Dave Johnston Power Plant

2.1.2.1 Expansion Landfill at Dave Johnston Power Plant

The expansion landfill is approximately a mile northeast of the plant, as shown in Figure 2.4. The landfill is used for the disposal of FGD scrubber waste, fly ash, and bottom ash. The landfill started to receive CCR in July 1993. The total landfill area comprises approximately 122.6 acres of land.

Figure 2.4 Dave Johnston Power Plant with the expansion landfill

2.1.3 Nucla Power Plant

The Nucla Station, operated by Tri-State Generation and Transmission, was a 113.8 MW coal-fired power station located near Nucla, Colorado. The power station retired in September 2019. Established in 1959, the plant had four units in operation—three units with 11.5 MW and one unit with 79.3MW, respectively. We went through a series of conversations with the personnel at Nucla Station and scheduled a virtual meeting that made us aware of the current situation of the station and landfill. Almost all the areas of the landfill have been covered by soil and vegetation. The project manager of the generation, David J. Braun, said that the route to the landfill would be very difficult since the roads were not fully developed. For these reasons, sample collection from the landfill was not possible, and we had to rely on the available samples supplied to us from Tri-State Generation and Transmission headquarters. The samples contained two five-gallon buckets of fly ash and bottom ash, respectively.

2.2 Observations and Findings with Sampling Plan

2.2.1 Sampling Plan

A proper method of sampling the fly ash data is shown in Figure 2.5. In this project, sampling method A had to be adopted because of the area constraints in the landfill. We had to break down the area of fly ash into two parts (we chose the area where fly ash did not contain many pebbles and had satisfactory quality as per visual inspection).

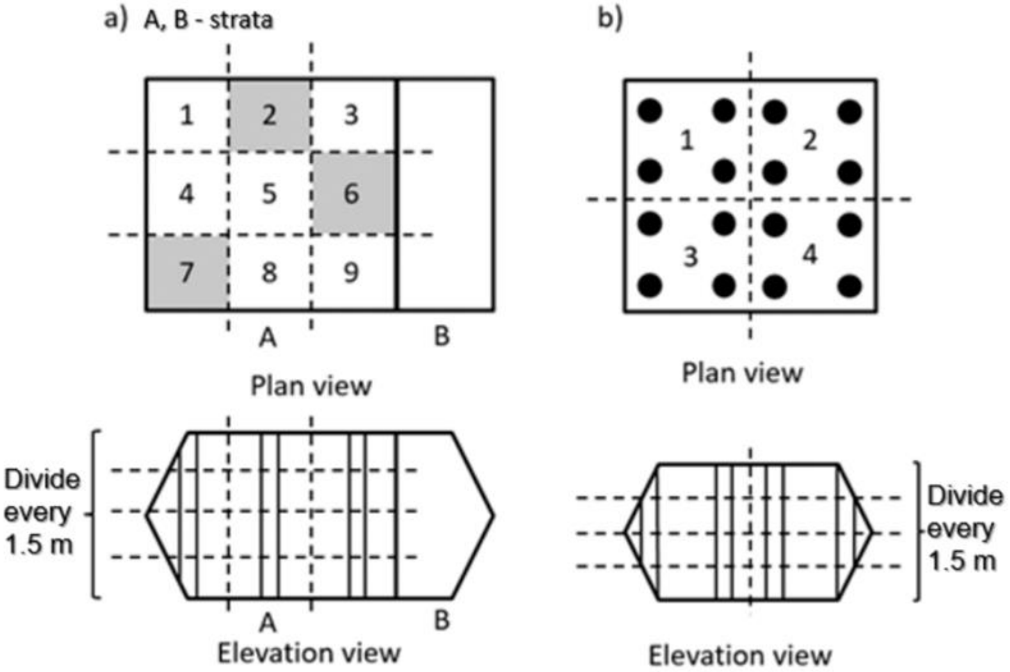

Figure 2.5 Left: Method A – stratified random sampling approach, Right: Method B – regular grid-based sampling

2.2.2 Jim Bridger Power Plant

During the visit, we observed that there were only three cells in the landfills actively receiving the fly ash, bottom ash, and mixed waste, respectively. The rest of the landfill was covered with a 2.5-ft. layer of topsoil and other waste materials. Hence, we could extract the samples from the three active cells only. Figure 2.6 represents the status of the landfill with active cells.

Figure 2.6 Industrial landfill with active cells

Note: We were restricted to use the drone or any other instruments to collect the aerial images of the landfill, which is why we had to rely on Google Earth images. This Google Earth image has not been updated since 2017, so, the landfill area at present is not the same as shown in the image.

We extracted samples from eight locations, as shown in the figure. From the eight locations, 14 samples were extracted. The samples for bottom ash and mixed ash were extracted from the center of the area covered by those materials. The details are summarized in Table 2.1.

Table 2.1 Summary information of collected samples from JB Power Plant

Location	Type	Number of Samples
A	Fly Ash	3
B	Fly Ash	1
C	Fly Ash	1
D	Fly Ash	1
E	Fly Ash	3
F	Fly Ash	1
G	Bottom Ash	1
H	Mixed Ash	3

Figure 2.7 Sampling plan of fly ash in Jim Bridger Power Plant

As shown in Figure 2.7, three samples in each part of the landfill were collected from the center. Other features were:

1. The bottom ash and fly ash are about a year old while the mixed ash is about 4–5 years old.
2. The fly ash is Class-F.

2.2.3 Dave Johnston Power Plant

During the visit, we observed that there was only one part of the landfill actively receiving the CCR. The landfill was in the overhaul process during the visit. The CCRs were being landfilled in layers of fly ash and bottom ash combined with no separate area for the disposal of fly ash or bottom ash, respectively. In most areas, the layer of fly ash was covered with a meter or deeper layer of bottom ash. However, some locations in the landfill had fly ash being compacted but not covered by bottom ash yet. Hence, we could extract the samples from such areas only. The extracted samples are not that old since all the old samples were covered and mixed by layers of bottom ash and other wastes. Two types of fly ash were being deposited in the landfill area. The types could be distinguished by visual inspection. The relatively lighter sample (whitish) had lime in it. The disposal of the ash was not systematically arranged.

Figure 2.8 Expansion landfill at Dave Johnston Power Plant

Note: 1 & 2–available landfill with landfilled fly ash; 3–overhaul of bottom and fly ash; 4–mixed ash (was not accessible); 5–not accessible area.

As shown in the figure, only two areas were available to extract the samples. We extracted samples from 14 samples from these two locations. Area 1 had diverse types of fly ash, and in some areas the fly ash was also mixed with some bottom ash, which is described in the sample log as well. There were two types of fly ash; the one with lime is marked as "Fly Ash 1" in the log; the one without lime is marked as "Fly Ash 2." Area 2 had fly ash without lime. The one mixed with bottom ash was distinguished through visual inspection. The bottom ash was brownish (as mentioned by plant personnel). The details are summarized in Table 2.2 below.

Table 2.2 Summary information of collected samples from DJ power plant

Location	Area	Type	Number of Samples
A	1	Fly Ash	3
B		Fly Ash	1
C		Fly Ash	1
D		Fly Ash	1
E		Fly Ash	1
F		Fly Ash	1
G		Bottom Ash	1
H	2	Fly Ash	1
I		Fly Ash	3
J		Fly Ash	1

2.2.4 Sampling Plan of Fly Ash in the Dave Johnston Power Plant

In Figure 2.9, samples from locations D, E, F, and G were distributed randomly, which is why a proper sampling plan could not be established at that part.

Figure 2.9 Sampling plan of fly ash in area 1

Figure 2.10 Sampling plan of fly ash in area 2

Three samples in each part of the landfill were collected from the center.
Other features included the following:

1. The bottom ash and fly ash are a few months old from area 1; the fly ash from area 2 is a year old.
2. The fly ash is Class C.

3. MATERIALS AND METHODS

3.1 Materials

3.1.1 Cementitious Materials

Five LFA samples were randomly selected from the collected LFA samples from three different active landfill sites: two samples from Dave Johnson (DJ) in Wyoming, two samples from Jim Bridger (JB) in Wyoming, and one sample from the Nucla power plant in Colorado. The samples consisted of two landfilled Class F fly ash samples (JB1 and Nucla), two landfilled Class C fly ash samples (DJ1 and JB2), and one landfilled bottom ash sample (DJ2). The particle size distribution of the collected landfill fly ash samples is illustrated in Figure 3.1.

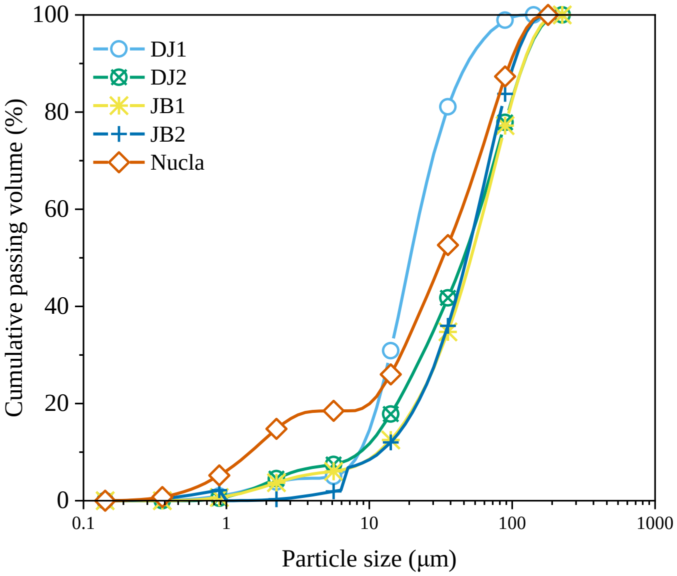

Figure 3.1 Volumetric particle size distribution of unbeneficiated LFAs

In addition, a type I/II ordinary Portland cement (OPC) and an ASTM C618-grade fly ash (FA) were included in the study for comparative analysis with the LFAs.

3.1.2 Aggregates

Three different types of sand were utilized in this study. For testing the strength of mortar specimens containing LFAs, a standard-graded sand from Humbolt that adhered to ASTM C788 standard [48] was employed. Conventional washed river sand, with a bulk specific gravity of 2,614 kg/m^3 and water absorption of 1.21%, was used to create specimens for measuring electrical resistivity and a rapid chloride penetration test. Highly reactive washed sand with the recorded expansion of 0.9% at 14 days according to ASTM C1260 [49], bulk specific gravity of 2,562 kg/m^3, and water absorption of 2.98% was used to make specimens for assessing resistance to alkali-silica reaction expansion.

3.2 Beneficiation Process

Figure 3.2 illustrates the summary of the decision-making process used for beneficiation in this study. Prior to the beneficiation process, the samples were dried if necessary and then passed through a No. 100

sieve with a nominal opening of 149 µm to remove any larger particles such as sand, coal, or other substances. Figure 1 presents the decision-making process employed in this study to identify the appropriate beneficiation method for each LFA. The main criteria considered were an LOI value below 3% and a particle size distribution in which at least 64% of the samples passed through a 45-µm sieve. It should be emphasized that ASTM C618 sets a maximum acceptable LOI of 6% for Class F and C fly ashes. Nonetheless, for this research, a lower threshold was chosen to examine its impact on enhancing the reactivity of LFAs.

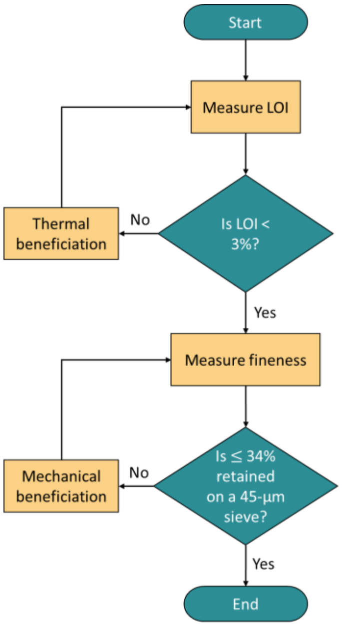

Figure 3.2 Flowchart illustrating the decision-making process for selecting beneficiation methods for different types of LFAs based on physicochemical characteristics

To determine the optimal temperature for thermal beneficiation, a parametric study was conducted. DJ2 LFA, which displayed the highest LOI, was divided into four portions, each weighing 5 g. These portions were then placed in individual crucibles and securely capped. Subsequently, the crucibles containing the LFA samples were subjected to heating at different temperatures: 350°C, 500°C, 600°C, and 700°C. The heating process took place for a duration of one hour within a muffle furnace. The LOI of the incinerated LFAs was then measured in accordance with ASTM C311 [50] to identify the temperature necessary to achieve an LOI below 3%. Based on the results shown in Figure 2, a temperature of 450°C was chosen for the thermal treatment of LFAs with an initial LOI exceeding 3%. Another parametric study was conducted to determine the optimal grinding duration for the LFAs that did not meet the fineness requirement of no more than 34% of particles remaining on a 45-micron sieve (sieve No. 325). For this purpose, approximately 500 grams of an oven-dried DJ2 LFA sample were placed inside a Micro-Deval jar (Gilson Inc.). For every 100 grams of ash, ten 9.5-mm diameter stainless steel balls were added to the jar, and it was rotated at 100 rpm for durations ranging from 15 to 90 minutes. After each 15-minute grinding interval, the fineness of the LFA sample was measured following ASTM C430 [51]. The results depicted in Figure 3.3 indicated that a grinding time of approximately 80 minutes was necessary to achieve the desired fineness.

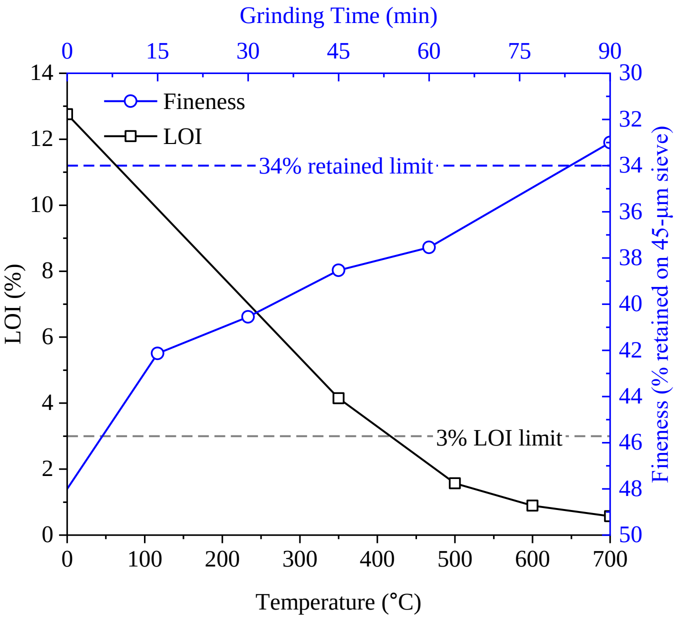

Figure 3.3 Heating temperature and grinding time optimization for LOI and fineness criteria limits of DJ2 LFA

3.3 Testing Methods

3.3.1 Chemical and Physical Characterization

The chemical composition of LFAs was determined through X-ray fluorescence (XRF) analysis in accordance with ASTM C114 standard [52]. For this purpose, one gram of the test sample was weighed and mixed with a flux at a mixing ratio of 1:2. The were thoroughly mixed, placed in a platinum crucible, and fused into a bead at 1,000°C using a fluxer (Classie, Leneo). The bead was later analyzed in an XRF machine (Axios, Panalytical). The LOI was determined in accordance with ASTM C311 [50] by incinerating 3 grams of LFA in a covered crucible at 750°C and 950°C for 45 minutes using a muffle furnace.

A carbon/nitrogen analyzer (CN802, VELP Scientific) was employed to measure the total carbon content in LFA samples. To achieve this, one gram of the ash sample was deposited into a crucible, which was subsequently inserted into the CN802 analyzer. The analyzer subjected the sample to heating within an oxygen-purged environment, raising the temperature to 1,030°C, thereby converting the entire sample into its constituent elemental forms. The instrument estimated the total carbon content by evaluating the concentration of CO_2 detected.

To assess whether the LFAs in this study underwent hydration as a result of exposure to lime and moisture in the landfills, thermal gravimetric analysis (TGA) was conducted using a TGA 55 instrument by TA Instruments. Approximately 35 mg of the LFAs were used for the TGA analysis. The TGA method involved incrementally increasing the temperature at a rate of 10°C per minute from ambient to 1,000°C in an inert nitrogen atmosphere. To measure the moisture content, 100 grams of LFA samples were heated in an oven at 110°C for 24 hours, following the ASTM C311 guidelines [50]. The fineness of the LFAs, represented as the percentage retained on a 45-µm sieve, was determined by wet-sieving 1 gram of LFA under a pressurized water stream of 69 kPa, following the ASTM C430 standard [51]. The median particle size (d_{50}) and specific surface area of the LFAs were measured using laser diffraction analysis with the Mastersizer 2000 equipment (Malvern Panalytical). A feed rate of 750 mg of LFA, at a rate of

35%, was utilized under 3.5-bar air pressure. The LFAs' densities were determined using a Le Chatelier flask filled with kerosene, following the ASTM C118 standard [53].

The crystallographic properties of LFAs were determined using X-ray diffraction (XRD) analysis. XRD patterns were recorded in the 2θ range of 10°–75° using a Bruker D8 Discover DaVinci X-ray diffractometer. The instrument was equipped with a Cu Ka X-ray source operating at 40 kV with a current of 40 mA. The XRD results were analyzed using the Bruker DIFFRAC EVA software (version 5.1.0.5), which incorporated the Crystallography Open Database (COD) [54, 55].

The scanning electron microscope (SEM) images were captured using the SEM JEOL 6500F instrument. Prior to imaging, the samples were coated with a conductive gold layer. Images were obtained at various magnifications, and the voltage applied was set to 5kV.

3.3.2 Reactivity Measurements

3.3.2.1 Modified R3 Test

When supplementary cementitious materials with pozzolanic properties are incorporated into cement, they consume the calcium hydroxide generated during cement hydration to form C-S-H, releasing heat in the process [56, 57]. This consumption of calcium hydroxide enhances the overall structure of the concrete and contributes to improved performance and durability. In this study, the pozzolanicity of LFAs was determined based on the modified R^3 (rapid, relevant, and reliable) test, which was originally proposed by Avet et al. [58] and later modified by Suraneni and Weiss [59]. In this test, $Ca(OH)_2$ powder and an SCM are mixed in an alkaline solution made with KOH, and the heat release is measured via calorimetry over the span of 7 to 10 days. The original test required adding carbonates [58] and sulfates [60] to the paste and maintaining the calorimeter at 40°C. However, to exclude the confounding effects of adding carbonates and sulfates on the hydrate phase assemblage and to expedite the hydration process, Suraneni and Weiss [32] excluded the addition of carbonates and sulfates and suggested performing the calorimetry at 50°C. After the completion of the calorimetry test, the paste sample is used for thermogravimetric analysis (TGA) to determine the amount of the $Ca(OH)_2$ still present in the paste. The difference between the initial and final $Ca(OH)_2$ content represents the amount of consumed $Ca(OH)_2$ as a result of the pozzolanic reaction.

To perform the modified-R^3 test in this study, one part LFAs was first dry mixed with three parts reagent-grade $Ca(OH)_2$ powder by mass [58, 59]. This mixture was then mixed with 0.5 M KOH solution at a liquid-solid mass ratio of 0.9. The materials were then hand mixed for four minutes before being transferred to a glass ampule. The ampule was then sealed and kept inside an isothermal calorimeter (TAM Air, TA instruments) for 10 days maintained at 50°C ± 0.05°C to measure the heat release. After 10 days, TGA was carried out using a Q500 TA Instrument 55 on about 20 mg of the paste powder to determine the consumed calcium hydroxide content. The TGA method involved ramping up the temperature at 20°C/minute from ambient to 500°C in an inert nitrogen atmosphere. The amount of calcium hydroxide content in the cementitious paste, expressed in grams per 100 grams of paste, was determined by calculating the mass loss within the temperature range of 350°C to 500°C using the tangential method [61]. The data were analyzed using TA Instruments TRIOS® software.

3.3.2.2 Degree of Reactivity Test

The degree of reactivity (DoR) indicates the extent of the reaction between calcium hydroxide and the pozzolanic material within a specified timeframe. It is expressed as a percentage, with higher values indicating greater reactivity. Assessing the DoR is crucial for evaluating the performance of SCMs in concrete, and it serves as an essential input parameter when simulating cement hydration in the presence of a material with pozzolanic properties [62-64]. In this study, the DoR of the LFAs was calculated using the proposed method by Bharadwaj et al. [65]. This method is based on considering the bulk chemical composition of SCMs from XRF analysis and the cumulative heat release in samples prepared for the modified R^3 test. According to this method, the degree of reactivity (DoR) of an SCM can be estimated using Eq. (1):

$$DoR = \frac{Q}{Q_{100}} \tag{1}$$

Where Q is the measured maximum cumulative heat release obtained from calorimetry test in the modified R^3 test and Q_{100} is the average heat released by an SCM of the given type at 100% DoR. Bharadwaj et al. [65-67] identified a range of values of Q_{100} for siliceous, calcareous, or silico-aluminous SCMs, depending on their chemical composition and the criteria shown in Eq. (2). These criteria obviate the need for researchers and industry practitioners to perform thermodynamic simulations and instead only require the chemical composition obtained from XRF results.

$$\begin{array}{lll} \text{Siliceous} & \text{CaO} < 50\% & \dfrac{\text{SiO}_2}{\text{SiO}_2 + \text{Al}_2\text{O}_3} > 70\% \\ \text{Calcareous} & \text{CaO} > 50\% & \dfrac{\text{SiO}_2}{\text{SiO}_2 + \text{Al}_2\text{O}_3} < 70\% \\ \text{Silico-aluminous} & \text{CaO} < 50\% & \dfrac{\text{SiO}_2}{\text{SiO}_2 + \text{Al}_2\text{O}_3} < 70\% \end{array} \tag{2}$$

3.3.3 Compressive Strength and Flow Test

The compressive strength of LFA-blended mortars was assessed using 50-mm cube specimens in accordance with ASTM C109 standard [68]. The mixes were prepared based on the proposed mixture proportion for the strength activity index test stated in ASTM C311 [50]. Table 3.1 provides a summary of the mixture proportion used for testing the compressive strength of samples. Eleven different mixes were made for OPC, standard fly ash, and unbeneficed and beneficiated LFAs. The control mix consisted solely of OPC cement with a water-to-cementitious material ratio (w/cm) of 0.48. In the remaining mixes, 20% of the cement mass was substituted with either FA or LFAs. The water content in the LFA-blended mixes was adjusted to ensure that the flow of the mix fell within ± 5% of the flow exhibited by the control mix.

The flow test, conducted following ASTM C1437 [69] guidelines, involved the placement of mortar into a flow cone positioned on a flow table in sequential layers. Each layer was compacted by tamping it 20 times to ensure consistent consolidation. Once the cone was filled, the flow table was promptly dropped 25 times mechanically within a 15-second timeframe. The resulting percent increase in mortar diameter, compared with the base diameter of the flow cone, was measured and expressed as the flow value.
Six cubes were prepared for each mix, resulting in 66 cubes. After molding, the specimens were placed in a moist room at a temperature of 23.0°C ± 2.0°C for 24 hours, with the surfaces protected to prevent water evaporation. Subsequently, the molds were removed, and the cubes were extracted. These cubes

were then immersed in a saturated lime solution, following the specifications outlined in ASTM C109 [68], until the testing day. Compressive strength measurements were conducted at 28 and 90 days to evaluate the strength development of the specimens.

Table 3.1 Mix proportion of compressive strength test. Six replicates were produced for each mix

Mix ID	Cement (g)	LFA (g)	Standard Sand (g)	Water (g)	Average flow diameter (in)	Flow (%)
OPC	500	0.0	1375	242	8.13	103%
FA	400	100	1375	250	8.30	108%
UDJ1	400	100	1375	260	8.25	106%
UDJ2	400	100	1375	260	7.93	98%
UJB1	400	100	1375	260	8.25	106%
UJB2	400	100	1375	260	8.28	107%
UNucla	400	100	1375	260	7.93	98%
BDJ1	400	100	1375	260	8.23	106%
BDJ2	400	100	1375	260	8.10	103%
BJB1	400	100	1375	250	8.28	107%
BJB2	400	100	1375	250	8.30	108%

3.3.4 Electrical Resistivity

To measure the bulk and surface electrical resistivities, cylindrical samples measuring 100×200 mm (diameter × length) were prepared using normal sand and the mix proportions specified in Table 3.2. One cylinder was cast for each mix. Once cast, the specimens were placed inside an environmental chamber, maintained at a temperature of 23°C and a relative humidity of 95% for 24 hours. The specimens were then removed from molds and kept inside a simulated pore solution in accordance with ASTM C1876. This solution was made by mixing 7.6 g of dry NaOH, 10.64 g of dry KOH, and 2.0 g of dry $Ca(OH)_2$, and then adjusting the volume to 1 using distilled water.

The electrical resistivity was assessed at 40 Hz using a four-electrode concrete resistivity meter with a 38-mm probe spacing. The bulk and surface electrical resistivity of the specimens were measured at regular intervals of 1, 3, 7, 14, 21, 28, 56, and 90 days. The surface resistivity was measured at eight different locations on the surface of each concrete cylinder. To determine the bulk resistivity (ρ) of the cylinders, they were positioned between two metal plates with a conductive foam sandwiched between the concrete and metal plate. The plates were then connected to the resistivity meter to measure the bulk resistance of the cylinders. Subsequently, the measured resistance was corrected using Eq. (3) to account for the probe spacing and geometry of the specimens.

$$\rho = \frac{R}{2\pi a} \times \frac{A}{L} \tag{3}$$

Where ρ is the resistivity (kΩ.cm), R is the resistance (kΩ.cm), a is the probe spacing (cm), which was 3.8 cm in this study, A is the cross-section area of the cylinder (cm^2), and L is the length of the cylinder (cm). The term A/L in Eq. (1) is often referred to as geometry constant k.

3.3.5 Rapid Chloride Ion Penetration Test

In order to assess the resistance of LFA-blended mortars to chloride penetration, an additional cylindrical specimen from each mixture listed in Table 3.2 was cast and subjected to the rapid chloride permeability test (RCPT) after 56 days of curing. For this purpose, a 100×50 mm specimen (diameter × length) specimen was extracted from the central region of 100×200 mm mortar cylinders using a wet masonry saw. Precise measurements of the samples were documented for accurate calculations. Following the cutting process, the surfaces of the specimens, except for the two ends, were coated with epoxy and left to dry overnight.

Next, the specimens were vacuum saturated for a period of 18 ± 1 hours, following the procedure outlined in ASTM C1202 [70]. Once the vacuum saturation was complete, the specimens were placed between two acrylic cells. One cell was filled with a 0.30 N NaOH solution, while the other contained a 3% NaCl solution. The cells were connected to a power source, and the current passing between the two cells was measured at one-minute intervals over a duration of six hours. The total charge passed during this test was used to classify the concrete according to ASTM C1202 [70], which assigns five categories ranging from negligible to high chloride permeability.

Table 3.2 Mix proportion for assessing the electrical resistivity, chloride ion penetration resistance, and water penetration of LFA-blended mortars. Two replicates were produced for each mixture

Mix ID	Cement (g)	LFA (g)	Normal sand (g)	w/cm
OPC	903.0	0.0	2461.2	0.5
FA	722.4	180.6	2461.2	0.5
BDJ1	722.4	180.6	2461.2	0.5
BDJ2	722.4	180.6	2461.2	0.5
BJB1	722.4	180.6	2461.2	0.5
BJB2	722.4	180.6	2461.2	0.5
UNucla	722.4	180.6	2461.2	0.5

3.3.6 Alkali-silica Reaction Expansion

To investigate the impact of LFA on ASR expansion mitigation, mortar bar specimens were prepared using prism molds measuring 25×25×285 mm with a water-cement ratio of 0.5, following the ASTM C1260 guidelines [49]. Three replicates were produced for each mixture. The mixture incorporated highly reactive sand and selected LFA, as specified in Table 3.3. After filling the molds, they were placed in an environmental chamber maintained at 23°C and a relative humidity of 95% for 24 hours. The specimens were completely soaked in water in plastic containers and then placed in an oven at 80°C for 24 hours. Initial measurements were taken using a length comparator with a digital dial indicator after drying the surface of each bar with a towel. Subsequently, the mortar specimens were transferred and immersed in a 1 M NaOH solution and stored in sealed containers inside an oven maintained at 80°C. The length of the specimens was consistently measured over a 14-day period. The expansion of each specimen at each measurement point was determined by calculating the difference between the initial measurement and the subsequent measurement. The average expansion of the three specimens from each mix was measured and reported as the expansion for the corresponding period.

Table 3.3 Mix proportion for alkali-silica reaction expansion test. Three replicates were produced for each mixture

Mix ID	Cement (g)	FA (g)	Reactive sand (g)	w/cm
OPC	440	0	990	0.5
FA	352	88	990	0.5
BDJ1	352	88	990	0.5
BDJ2	352	88	990	0.5
BJB1	352	88	990	0.5
BJB2	352	88	990	0.5
UNucla	352	88	990	0.5

3.3.7 Rate of Absorption of Water

The rate of water absorption, known as the sorptivity of concrete samples, was evaluated following the guidelines outlined in ASTM C1585 [71]. The objective of this test was to determine how quickly water is absorbed by the concrete by monitoring the increase in specimen mass over a specific timeframe, up to nine days. Water absorption is significant in evaluating concrete durability as it indirectly measures the porosity of the concrete that is accessible to water [72]. For this purpose, 100×200 mm cylinders were cast following the mixture proportion provided in Table 3.2 and cured for 28 days in lime water. Specimens measuring 100×50 mm were then cut from the center of the cured 100×200 mm cylinders. Before initiating the absorption procedure, the test specimens underwent conditioning. They were initially saturated in a vacuum chamber and subsequently placed in an environmental chamber with a temperature of 50°C and a relative humidity of 80% for three days. After this conditioning period, each specimen was sealed with wrapping plastic and placed in a container, which was then stored at a room temperature of 23.0°C ± 2.0°C for 15 days. After the 15-day storage period, the weight of the specimens was recorded. The specimens were then immersed in a container of water, ensuring that the bottom 2 mm of each specimen was submerged. The mass of the specimens was measured on the 2nd, 3rd, 7th, 10th, and 14th days in accordance with the guidelines specified in ASTM C1585 [71]. The absorption in each sample was measured using Eq. (4).

$$I = \frac{m_t}{a \times \rho_w} \tag{4}$$

where, I is the absorption expressed in mm, m_t is the change in the specimen mass in grams, at time t, a is the exposed surface area of the specimen in mm^2, and ρ_w is the density of water in g/mm^3 (0.001 g/mm^3). The initial rate of water absorption was calculated by fitting a linear regression model to the data and determining the slope of the line that fits the data for the first six hours of testing. The initial absorption of the concrete is also known as "sorptivity." Furthermore, the secondary rate of water absorption was measured by fitting a linear regression model to the data from days one to seven.

4. RESULTS

4.1 Physical and Chemical Properties of Unbeneficiated LFAs

Information associated with the chemical composition, LOI (at 750°C), total carbon content, moisture content, fineness, median particle size, specific surface area, and density of LFAs, are provided in Table 4.1 and 4.2. According to the chemical composition of LFAs presented in Table 4.1, the combined proportions of SiO_2, Al_2O_3, and Fe_2O_3 for LFAs ranged from 60.1% in DJ1 to 85.9% in JB1. In contrast, the reference fly ash demonstrated a SiO_2+ Al_2O_3+ Fe_2O_3 value of 82.8%. Note that all LFAs investigated in this study met the ASTM C618 requirement for SiO_2+ Al_2O_3+ Fe_2O_3, exceeding 50% for both Class C and Class F fly ashes.

Regarding the CaO content, both DJ1 and JB2 showed similar values at approximately 25%, while DJ2 exhibited a CaO content of 21.33%. Nucla possessed the highest CaO content at 11.46%, which was still below the maximum threshold of 18% specified by ASTM 618for Class F fly ash. Regarding the SO_3 content, DJ1 and JB2 once again showed similar values of 1.28% and 1.31%, respectively, which were considerably lower than the maximum allowable limit of 5% specified by ASTM C618 for Class C and F fly ashes. Nucla had the highest SO_3 content at 4.4%, which still fell within the acceptable range. Similarly, DJ2 with an SO_3 content of 2.2% met the requirement set by ASTM 618. The total alkali content (Na_2O+K_2O) of LFAs ranged from 1.25% to 2.48%, which were all significantly lower than that of the reference fly ash.

Table 4.1 Chemical composition of materials used in this study. The symbol "–" means not applicable or not reported in the product mill sheet

ID.	Oxide composition (% mass)								
	SiO_2	Al_2O_3	Fe_2O_3	CaO	MgO	SO_3	Na_2O	K_2O	LOI
OPC	19.24	3.8	2.75	59.05	1.5	2.49	0.17	0.6	9.9
FA	54.24	18.16	10.42	7.37	1.46	1.3	1.24	2.71	1.13
DJ1	37.05	17.52	5.49	25.26	4	1.28	0.86	0.46	4.89
DJ2	37.1	14.91	4.77	21.33	3.39	2.2	0.73	0.52	12.76
JB1	65.55	15.17	5.18	5.76	1.86	0.47	1.36	1.12	1.55
JB2	37.47	17.55	5.48	25.09	3.98	1.31	0.91	0.45	4.7
Nucla	50.3	23.61	2.76	11.46	0.93	4.4	0.47	0.9	2.5

Table 4.2 Physical properties of OPC, ASTM C618 Class F fly ash (FA), and as-received LFAs

ID	Total carbon (%)	Moisture content (%)	Percent retained on 45 µm	d_{50} (µm)	Specific surface area (m^2/kg)	Density (g/cm^3)
OPC	–	0	3.5	NR	NR	3.15
FA	–	0.03	17.79	16.34	597.90	2.39
DJ1	0.92	3.5	37.7	19.34	557	2.78
DJ2	13.13	23.5	49.51	45.84	441	2.47
JB1	0.54	3.5	45.98	51.52	386	2.33
JB2	1.05	2.5	54.28	20.85	466	2.36
Nucla	4.73	2.5	23.0	32.75	1300	2.56

Table 4.2 indicates that, with the exception of JB2 and Nucla LFAs, the moisture contents of the remaining LFAs exceeded the 3% limit set by ASTM C618. Among them, DJ2 had the highest moisture content of 23.5%. As a result, DJ1, DJ2, and JB1 LFAs required oven-drying. Regarding the LOI values, all LFAs, except for DJ2, had an LOI below the maximum threshold of 6%. However, for this study, a stricter LOI threshold of 3% was chosen, leading to the thermal beneficiation of LFAs from DJ1, DJ2, and JB2. For long-term stored fly ash in a high-moisture environment, fly ash may undergo some pozzolanic reactions with the lime in the environment. Therefore, not all the measured LOI can be associated with unburned carbon content with certainty. Figure 4.1 shows the TGA and derivative thermogravimetry (DTG) performed on the as-received LFAs. Notably, the materials responsible for LOI in both inert and reactive atmospheres (e.g., air) differ [73, 74]. Specifically, carbon does not undergo oxidation in the presence of nitrogen; however, it can be transformed into CO or CO_2 through reactions involving the reduction of iron and sulfur compounds at temperatures above 700°C [46, 74-76]. Therefore, distinguishing between the decomposition of hydrated phases and the reduction of iron and sulfate can be challenging.

The mass loss between 100°C to 150°C in Figure 3 can be attributed to the evaporation of free water and the water released during the conversion of gypsum to hemihydrate and subsequently to anhydrite [77]. Additionally, a significant mass loss associated with the release of water from portlandite is observed between 400°C to 500°C [77]. Between 570°C and 635°C, the mass loss can be linked to the decomposition of mono- or hemi-carbonates or the reduction of iron oxide by organic carbon [74, 77]. The decomposition of calcite can be observed around 720°C. Around the same temperature range, starting at 650°C and continuing up to 700°C, ferric oxide (Fe_2O_3) undergoes reduction to form magnetite (Fe_3O_4), subsequently transitioning to ferrous oxide above 900°C [73, 74]. The additional dehydroxylations at about 800°C can also be related to the decomposition of C-S-H to wollastonite [77]. Table 2 reveals that the total carbon content of ashes ranged from 18% to 100% of the measured LOI, indicating that the LFAs were probably hydrated due to exposure to lime and moisture, and the remaining portion of LOI can be attributed to the decomposition of hydration products such as portlandite and carbonates.

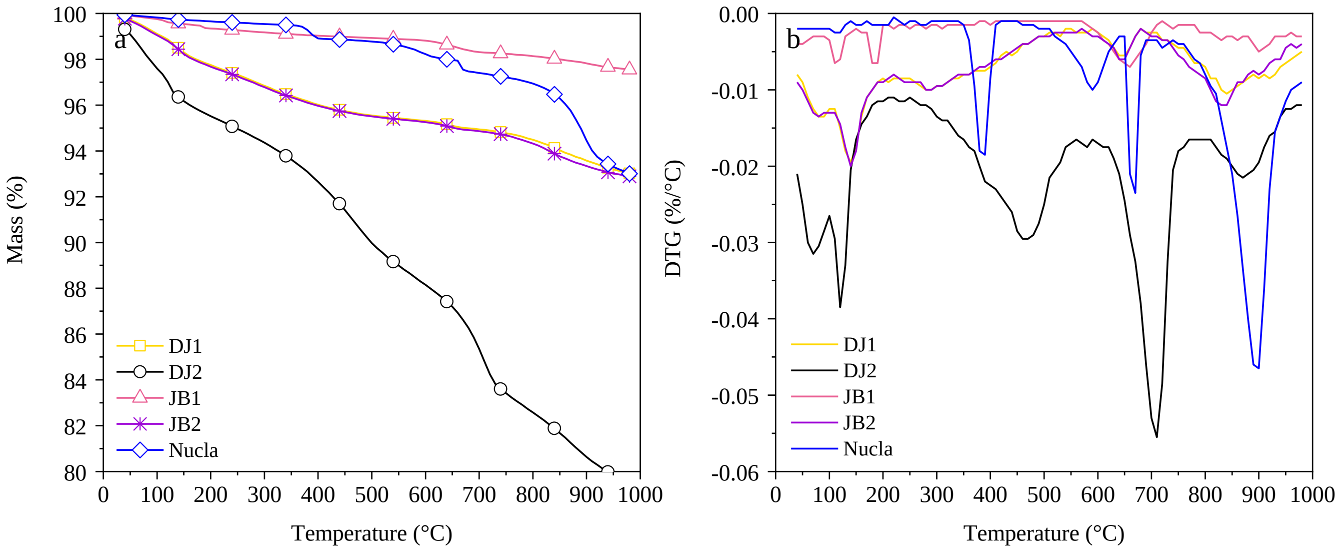

Figure 4.1 TGA and DTG of unbeneficiated LFAs

Among the LFAs examined, JB2 LFA exhibited the lowest fineness, with 54.28% of ash retained on the 45-µm sieve. Conversely, Nucla LFA demonstrated the highest fineness, with only 23% retained. The fineness order of the LFAs, from lowest to highest, was JB2 < DJ2 < JB1 < DJ1 < Nucla. Consequently, with the exception of Nucla ash, the other LFAs required mechanical grinding to increase their fineness. The d_{50} and specific surface area of the LFAs generally correlated with the results obtained from the fineness measurements using the 45-µm sieve method. The d_{50} of LFAs ranged from 19.34 µm in DJ1 to 51.52 µm in JB1, following the order of DJ1 < JB2 < Nucla < DJ2 < JB1. Interestingly, Nucla LFA, despite having the highest fineness based on the 45-µm sieve method, had the third smallest particle size, which deviated from the expected size order. However, the specific surface area of Nucla LFA aligned well with the measurements obtained from the 45-µm sieve method. The specific surface area of the LFAs ranged from 386 m^2/kg in JB1 to 1,300 m^2/kg in Nucla, following the order of JB1 < DJ2 < JB2 < DJ1 < Nucla.

Table 4.3 provides an overview of the extent to which the physical and chemical requirements of ASTM C618 were met, as well as the criteria employed in this study. The results indicated that DJ1, DJ2, and JB2 necessitated both thermal and mechanical beneficiation due to their coarse particle size and high LOI, whereas JB1 only required mechanical beneficiation since its LOI was below the 3% limit used in this study. As the LOI and fineness of Nucla LFA met the maximum limits of 3% and 34%, respectively, no beneficiation procedure was conducted on this particular LFA.

Table 4.3 Beneficiation recommendations based on chemical and physical requirements. The symbol "=" means same requirements as ASTM C618

Criteria	ASTM C618-23		This study	DJ1	DJ2	JB1	JB2	Nucla
	Class	Class						
Chemical requirements								
$SiO_2 + Al_2O_3 + Fe_2O_3$, minimum %	50	50	=	✓	✓	✓	✓	✓
CaO, %	≤18	>18	=	✓	✓	✓	✓	✓
SO_3, maximum %	5	5	=	✓	✓	✓	✓	✓
Moisture content, maximum %	3	3	=	✗	✗	✗	✓	✓
Max LOI (%)	6	6	3	✗	✗	✗	✗	✓
Physical requirements								
Fineness (% retained on 45-µm sieve), maximum	34	34	=	✗	✗	✗	✗	✓
Water requirement, maximum % of control	105	105	=	✗	✗	✗	✗	✗
Is Beneficiation required?								
Drying				✓	✓	✓	✗	✗
Thermal				✓	✓	✗	✓	✗
Mechanical grinding				✓	✓	✓	✓	✗

4.2 Effect of Beneficiation on the Crystalline Structure and Specific Surface Areas of LFAs

Figures 4.2a and 4.2b demonstrate that the impact of thermo-mechanical beneficiation on the mineral composition of LFAs is minimal. Both figures indicate that quartz and merwinite ($Ca_3Mg(SiO_4)_2$) were the primary crystalline phases found in all LFAs. XRD analysis revealed the presence of mullite ($3Al_2O_3.2SiO_2$) and hematite (Fe_2O_3) peaks in the unbeneficiated DJ1, DJ2, Nucla, and JB LFAs, with Nucla and JB LFAs showing a lower intensity. Furthermore, a small quantity of microcline ($KAlSi_3O_8$) was detected in the bottom ash from DJ2. Only the beneficiated DJ1 and DJ2 sample exhibited the presence of hematite. XRD analysis did not identify any signs of microcline in the DJ2 sample after it underwent the beneficiation process.

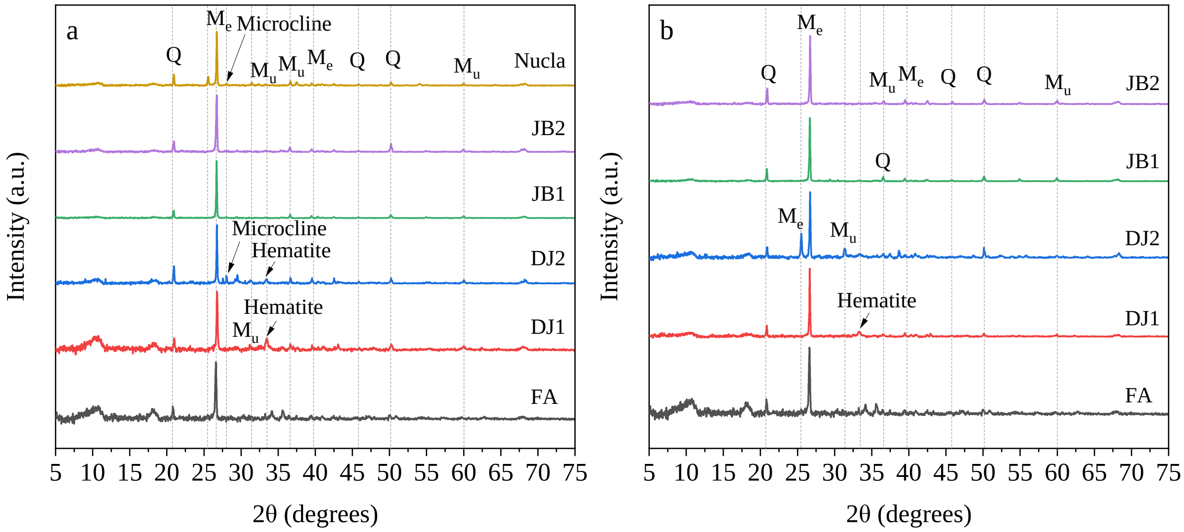

Figure 4.2 X-ray diffraction patterns of standard and landfilled fly ashes. Q: quartz, M_e: merwinite, M_u: mullite. (a) unbeneficiated, (b) beneficiated.

Figure 4.3 shows the influence of thermo-mechanical beneficiation on the specific surface area of LFAs. Among the four LFA sources that underwent beneficiation, DJ2 stood out with a significant increase of approximately 317% in specific surface area after beneficiation. This remarkable enhancement can be attributed to the porous and brittle nature of bottom ash [20, 78], along with the combined effect of thermal and grinding processes, which effectively broke down the particles, reducing their size and increasing the overall surface area of the bottom ash. Note that bottom ash is generally coarser and heavier than fly ash. Although there is no study specifically comparing the breaking of particles between bottom ash and fly ash when subjected to the same conditions in a ball mill, the size, density, hardness, and composition of the material can influence the resulting particle size distribution. DJ1, JB1, and JB2 also experienced notable increases in specific surface area after beneficiation, with percentage increases of 29%, 15%, and 25%, respectively. These improvements suggest that the beneficiation processes successfully enhanced the fineness of all the sources by reducing particle size and potentially increasing their reactivity.

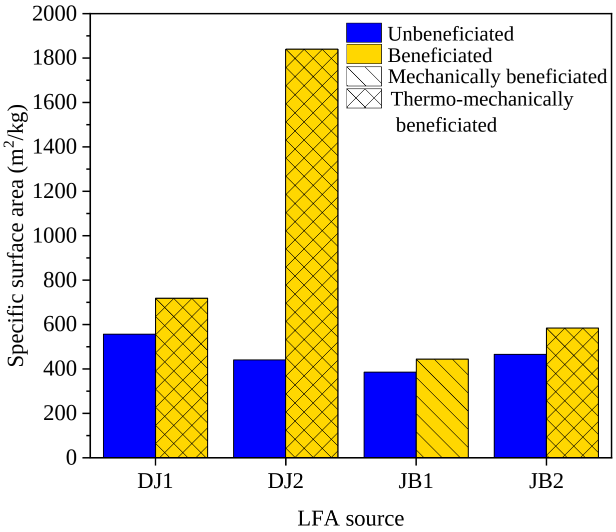

Figure 4.3 The influence of beneficiation on LFA specific surface area

Figure 4.4 illustrates the SEM images of reference fly ash and beneficiated LFAs. The combustion temperature and cooling rate significantly influence the morphology and crystalline structure of fly ash particles [79, 80]. The majority of LFA particles were in the size range of approximately 10 to 100 μm and exhibited solid spheres and irregularly shaped unburned carbon particles. The morphology of ash particles in JB1 and JB2 closely resembled that of the reference fly ash, albeit with larger particles. Other LFAs displayed varying degrees of roughness and angularity in their particles. Additionally, minerals and mineral aggregates, such as quartz, were often observed on the particle surface as melted spots [81]. Some LFAs showed agglomerated particles and irregularly shaped amorphous particles, which can be attributed to rapid cooling [81-83]. The Nucla LFA, which met the LOI and fineness requirements of ASTM C618, primarily consisted of irregular amorphous particles, likely resulting from inter-particle contact or rapid cooling [81].

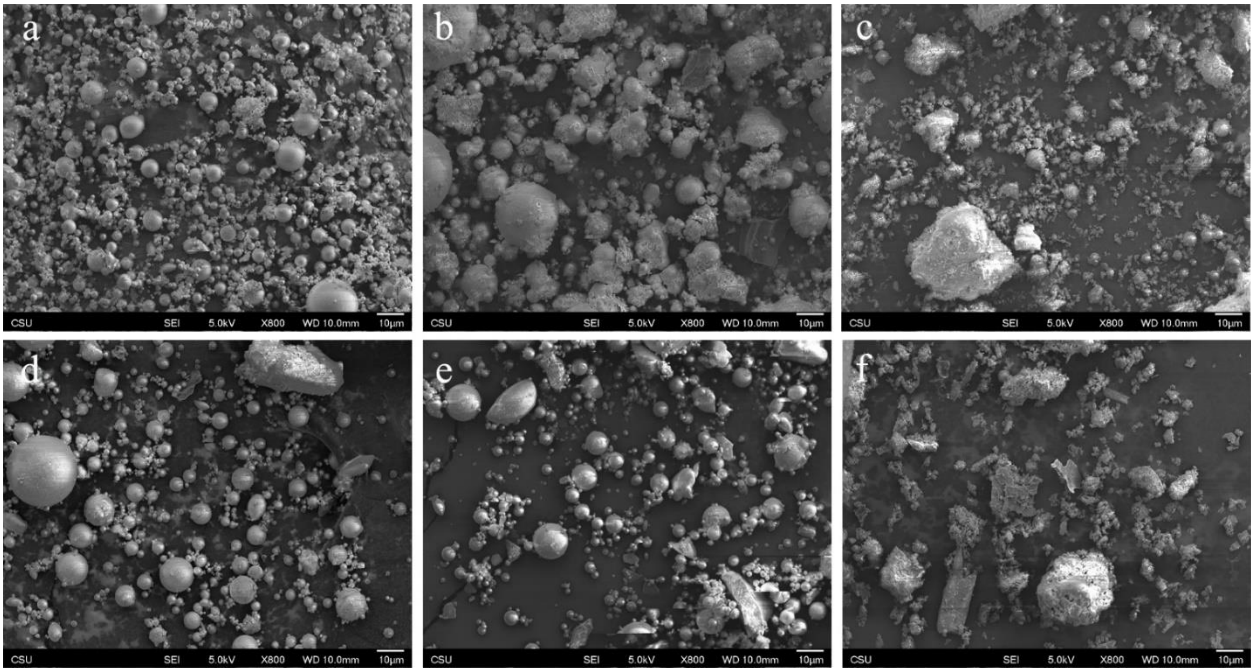

Figure 4.4 SEM images of standard FA and LFAs. (a) standard FA, (b) beneficiated DJ1, (c) beneficiated DJ2, (d) beneficiated JB1, (e) beneficiated JB2, (f) unbeneficiated Nucla

4.3 Modified R3 Test Results

Figure 4.5 shows the cumulative heat of hydration measurements of the model system at the 10-day mark. Among the unbeneficiated LFAs, the heat release values showed significant variation. The bottom ash from DJ2 exhibited a heat release value of 113.92 J/g SCM, while Nucla demonstrated the highest heat release of 359.22 J/g SCM. In comparison, the reference fly ash had a heat release value of 285.97 J/g SCM, which was approximately 26% lower than the Nucla LFA. The observed differences in heat release can be attributed to various factors, including the aluminate content and specific surface area of the LFAs. DJ2, with its lower aluminate content and specific surface area, exhibited a lower heat release compared with other LFAs and the reference fly ash. On the other hand, Nucla LFA displayed a higher heat release, potentially due to its significantly higher aluminate content and specific surface area. These factors influence the pozzolanic activity of the LFAs and their ability to consume calcium hydroxide.

Figure 4.5 shows that beneficiating the LFAs, on average, resulted in an 8% increase in heat release. Notably, DJ2 experienced the highest increase in reactivity with a remarkable 23.7% boost, while JB2 showed the lowest increase of only 0.4%. This indicates that the thermomechanical beneficiation process had a positive impact on the LFAs, improving their pozzolanic reactivity and ability to consume calcium hydroxide. Despite the improved reactivity achieved through beneficiation, LFAs still exhibited lower heat release values compared with the reference fly ash.

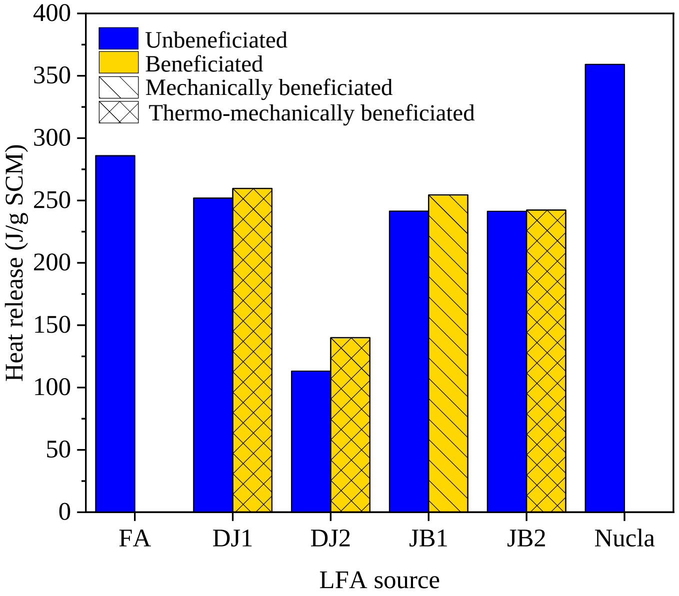

Figure 4.5 The influence of thermo-mechanical beneficiation process on the cumulative heat release measured based on the modified-R^3 test

Figure 4.6 shows that among the unbeneficiated LFAs, DJ1 exhibited the lowest $Ca(OH)_2$ consumption with a value of 23 g/100 g SCM, likely due to its lower silica content and higher CaO content. On the other hand, Nucla had the highest $Ca(OH)_2$ consumption with a value of 76.4 g/100 g SCM, surpassing the sample made with reference fly ash by 57%. The bottom ash from DJ2, with a consumed $Ca(OH)_2$ value of 27.83 g/100 g SCM, had the second lowest $Ca(OH)_2$ consumption. The JB samples demonstrated, on average, double the $Ca(OH)_2$ consumption compared with the DJ samples. The fineness of DJ and JB LFAs was similar, suggesting that the DJ LFAs may contain a higher proportion of inert materials.

It is crucial to note that DJ1, DJ2, and JB2 LFAs contained 25.26%, 21.33%, and 25.09% CaO, respectively, which were significantly higher (242%, 189%, and 240% higher, respectively) than the CaO content in the reference fly ash. The excess lime content in these LFAs, typically added during compaction in landfill areas, can explain their lower $Ca(OH)_2$ consumption. Additionally, the silica content in these three LFAs was approximately 37% by mass, while the silica content in Nucla, JB1, and reference fly ash was 65.5%, 50.3%, and 54.2%, respectively. Consequently, a portion of the higher $Ca(OH)_2$ consumption in LFAs with a higher silica content can be attributed to a higher likelihood of pozzolanic reaction between $Ca(OH)_2$ and silica, resulting in the formation of C-S-H.

The results presented in Figure 8 demonstrate the positive impact of thermo-mechanical beneficiation on increasing $Ca(OH)_2$ consumption. On average, the data revealed a remarkable 40% increase in $Ca(OH)_2$ consumption in beneficiated LFAs compared with their unbeneficiated counterparts. Among the beneficiated LFAs, JB2 exhibited the lowest increase with a modest 12.1% rise in $Ca(OH)_2$ consumption. On the other hand, DJ2 showcased the highest increase of 74.5%, indicating a significant enhancement in $Ca(OH)_2$ consumption. The notable increase in $Ca(OH)_2$ consumption in DJ2 can primarily be attributed to two factors resulting from thermomechanical beneficiation. First, thermal beneficiation effectively removed excess unburned carbon, which is known to have a negative influence on the reactivity of LFAs [84-86]. By eliminating this unburned carbon, the reactivity and ability of the LFA to consume $Ca(OH)_2$ are greatly improved, leading to increased $Ca(OH)_2$ consumption. Second, the grinding process during beneficiation significantly increased the fineness of the ash, as demonstrated in Figure 5. Fineness plays a crucial role in enhancing the reactivity of LFAs. The finer the particles, the greater the surface area available for chemical reactions. Consequently, the finely ground ash particles in DJ2 had a higher chance of reacting with $Ca(OH)_2$, leading to increased $Ca(OH)_2$ consumption.

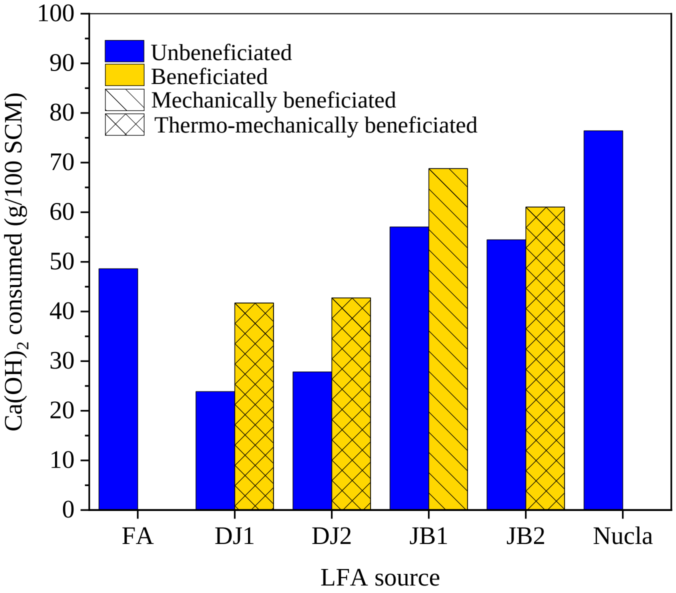

Figure 4.6 The influence of thermo-mechanical beneficiation on calcium hydroxide consumption in the modified-R^3 test

4.4 Degree of Reactivity

Figure 4.7 illustrates the correlation between cumulative heat release, as measured in the modified R^3 test, and the predicted DoR value based on the method proposed by Bharadwaj et al. [24]. According to Eq. (2), the LFA samples from DJ1, JB2, and Nucla were classified as silico-aluminious materials ($SiO_2/SiO_2+Al_2O_3$ <70%); whereas DJ2, JB1, and the reference fly ash were considered to be silicious ($SiO_2/SiO_2+Al_2O_3$ >70%). Analyzing the predicted DoR values of LFAs revealed a range from 14.1% in unbeneficiated ash from DJ2 to 51.4% in unbeneficiated ash from the Nucla plant. The average predicted DoR value of LFAs was 30.9% with a moderate level of variation, as indicated by the standard deviation of 11%. The results show that thermo-mechanical beneficiation increased the DoR value of the LFA by an average of 8.1%, with the lowest increase of 0.4% observed in JB2 and the highest increase of 23.7% observed in DJ2. As mentioned earlier, the substantial positive impact of beneficiation on the DJ2 sample can be attributed to a significant reduction in its LOI and an increase in its fineness.

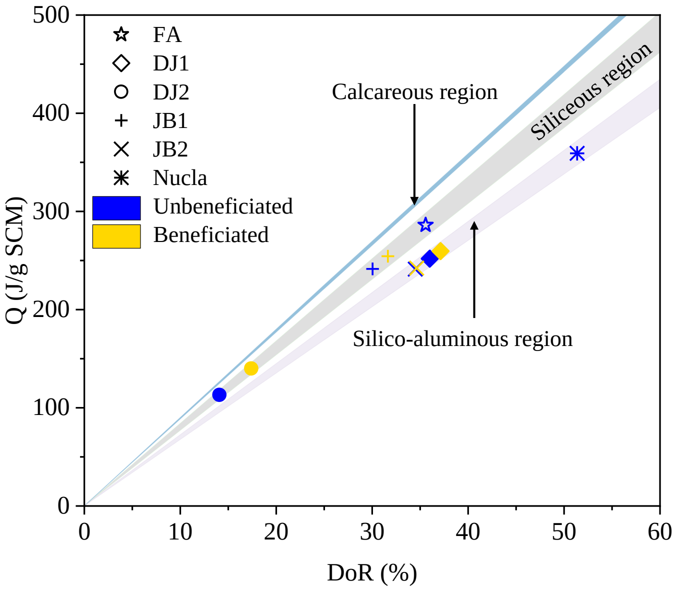

Figure 4.7 The predicted degree of reactivity of LFAs based on PRT method

4.5 Compressive Strength Results

Figure 4.8 illustrates the compressive strength results of mortar cubes containing unbeneficiated LFAs, alongside neat OPC and FA-blended specimens for comparison. At 28 days, the compressive strength values exhibited a significant range, varying from 21.76 MPa for UJB1 to 40.20 MPa for OPC. When comparing the compressive strength of LFA specimens with that of OPC, UNucla exhibited the highest compressive strength of 39.9 MPa, representing more than 99% of the OPC and 11% higher than FA. Similarly, UDJ1 demonstrated promising performance with a strength of 33.49 MPa, equivalent to 83% of OPC. However, UDJ2, UJB1, and UJB2 exhibited lower early strength, achieving compressive strengths of 28.2 MPa, 21.8 MPa, and 24 MPa, respectively, all falling below the minimum 75% of OPC strength required by ASTM C618 [26].

The 90-day compressive strength results showed an average increase of approximately 31.7% for all specimens. The measured 90-day compressive strength of mortar cubes ranged from 32.9 MPa for UJB1 to 54.2 MPa for Nucla. OPC experienced the lowest strength gain at 15.8%, while UJB1 showed the highest increase at 51.1%. These results reaffirm the fundamental mechanisms of later-age strength gain when fly ash is incorporated into the mix.

At 90 days, both Nucla and UDJ1 exhibited excellent performance with strength activity indices (SAI) of 116.5% and 84.7%, respectively, surpassing the 75% SAI requirement set by ASTM C618. UDJ2 marginally missed the minimum strength requirement with an SAI of 74.3%, indicating the potential for further improvement in its performance. UJB1 and UJB2 also showed promising results, coming remarkably close to meeting the 75% threshold, with SAIs of 70.6% and 73.4%, respectively.

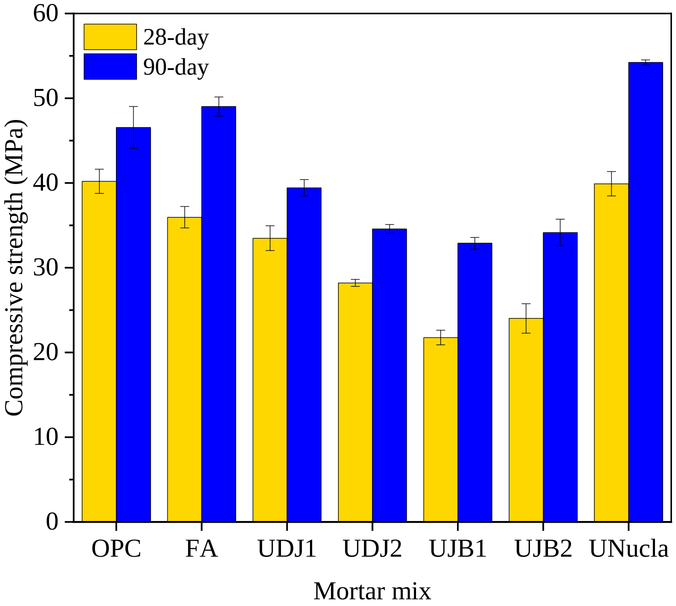

Figure 4.8 Compressive strength of OPC, FA, and unbeneficated LFA mortar specimen

Figure 4.9 compares the 28- and 90-day compressive strength of mortars containing beneficiated LFAs with neat OPC and a mix with ASTM C618-compliant fly ash. At 28 days, the compressive strength values for the mixes ranged from 31.38 MPa to 40.20 MPa, with OPC once again showing the average highest strength. The beneficiated LFAs, BDJ1, BDJ2, BJB1, and BJB2, all demonstrated competitive strength levels compared with OPC, achieving 86%, 78%, 79%, and 81% of its strength, respectively. These results align with previous studies, indicating that the inclusion of ASTM 618-compliant fly ash can reduce early concrete strength. This reduction is primarily attributed to a dilution effect and a slower rate of fly ash hydration compared with cement [87-89].

As the curing period extended to 90 days, the compressive strength of all mixes increased, as expected. OPC exhibited a strength gain of 6.36 MPa (15.8%) from 28 to 90 days, in line with typical cement hydration behavior. While BDJ2 showed a slightly lower 90-day strength compared with BDJ1, BJB1, and BJB2, it still maintained a strength level of 84% of OPC. At 90 days, the compressive strength of BDJ1, BDJ2, BJB1, and BJB2 was comparable to that of the standard fly ash. BDJ1, BDJ2, BJB1, and BJB2 achieved 87%, 83%, 80%, and 85.6% of the 90-day strength of standard fly ash specimens, respectively. These results highlight the potential of beneficiated LFAs as viable and sustainable alternatives to the ASTM C618-compliant fly ash in concrete production. The competitive strength performance of BDJ1, BDJ2, BJB1, and BJB2 compared to FA suggests that the beneficiation process successfully enhanced their pozzolanic properties. Therefore, the utilization of beneficiated LFAs can offer significant benefits in terms of strength performance.

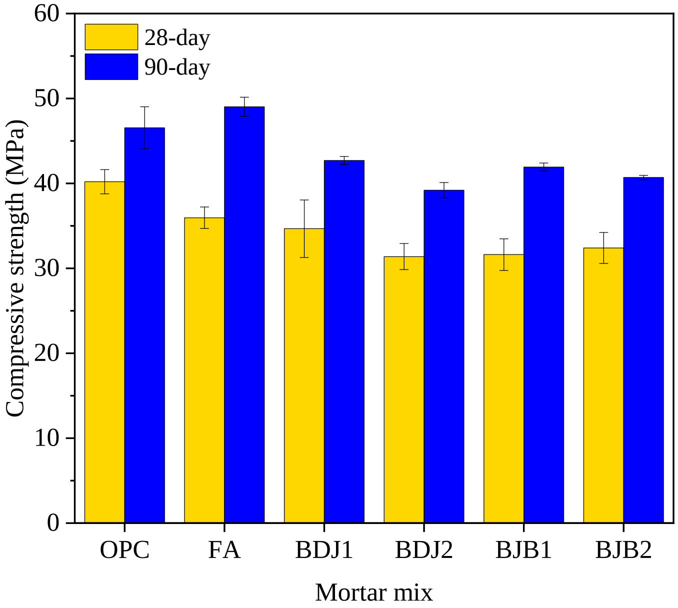

Figure 4.9 Compressive strength of OPC, FA, and beneficiated LFA mortar specimen

4.6 Bulk and Surface Electrical Resistivity Results

Bulk electrical resistivity assesses the material's overall quality and resistance to ingress of harmful elements, while surface electrical resistivity indicates the concrete's susceptibility to aggressive agents and potential vulnerabilities at its outer layer [90, 91]. These properties are crucial in evaluating concrete durability as they reveal potential deterioration mechanisms that can impact the material's long-term structural integrity and performance.

Figure 4.10a shows the bulk electrical resistivity values of the mortar specimens at different time intervals. Bulk electrical resistivity is a critical parameter in concrete as it provides insights into the material's resistance against the ingress of harmful species, consequently affecting its durability and performance over time. Overall, Figure 4.10a shows a clear increasing trend in resistivity as the mortar cured and gained strength over time. The results show that during the first 56 days of curing, BDJ1, BDJ2, BJB1, and BJB2 consistently exhibited lower bulk electrical resistivity values compared with OPC. However, the pattern changed after 56 days of curing. The results show that BDJ1, BDJ2, BJB1, and BJB2 exhibited higher resistivity values than OPC. On the other hand, UNucla consistently demonstrated higher bulk electrical resistivity than both OPC and FA mixes throughout the entire testing period. This indicates that UNucla was probably more reactive than FA, and the pozzolanic reaction in the specimen containing this ash started faster.

The observed shift in resistivity could be attributed to the development of various hydration products resulting from pozzolanic reactions [92]. Additionally, changes in the microstructures of these specimens may have also contributed to the observed increase [93]. Note that landfilled fly ash may exhibit variations in chemical composition, particle size, and carbon content, which can impact the electrical resistivity of concrete [94]. Due to the presence of unburned carbon particles that are electrically conductive, incorporating LFA with a higher LOI can lead to a reduction in the electrical resistivity of concrete.

At 90 days, the FA specimen displayed a resistivity of 49.1 Ω.m, approximately 110% higher than OPC. Among LFA-blended mixes at 90 days, BDJ2 demonstrated the lowest resistivity, measuring 31.1 Ω.m, which was approximately 25% higher than the resistivity of OPC at the same age. Following closely, both BDJ1 and BJB2 had similar resistivity values of 41.6 Ω.m, showing an approximately 78% increase compared with OPC. Meanwhile, BJB1 exhibited a resistivity of 50.1 Ω.m, approximately 115% higher than OPC. UNucla displayed the highest bulk electrical resistivity among all mixes at 90 days, measuring 82.2 Ω.m, which was approximately 252% higher than the resistivity of OPC at the same age. These results confirm the significant influence of different mix compositions on the mortar's electrical properties. The findings are consistent with the literature, which suggests that the addition of reactive supplementary cementitious materials like FA and LFA can lead to lower permeability and higher long-term electrical resistivity due to the reduction in capillary porosity and hydroxyl ions (OH^-) [93, 95-97].

Comparing the rate of change in bulk electrical resistivity of mixes can also provide useful insights regarding the kinetics of hydration and changes in the microstructure of the various mixes. Figure 4.10b shows that during the early days (up to around seven days), OPC exhibited the fastest rate of increase, and FA showed the slowest. However, after approximately 14 days, UNucla, along with FA, began to display the highest rate of increase compared with the other specimens. After day 28, the rate of increase in the bulk electrical resistivity of specimens started to plateau, reaching a constant rate ranging from 0.18 Ω.m/day in OPC to 0.66 Ω.m/day in FA specimens. Interestingly, after 56 days, the rate of increase in the bulk electrical resistivity of OPC specimens reached zero, while specimens containing FA and LFAs still had a positive rate. This confirms the ongoing pozzolanic reactions in samples containing FA and LFAs, which in turn affects the microstructure and bulk electrical resistivity of these specimens.

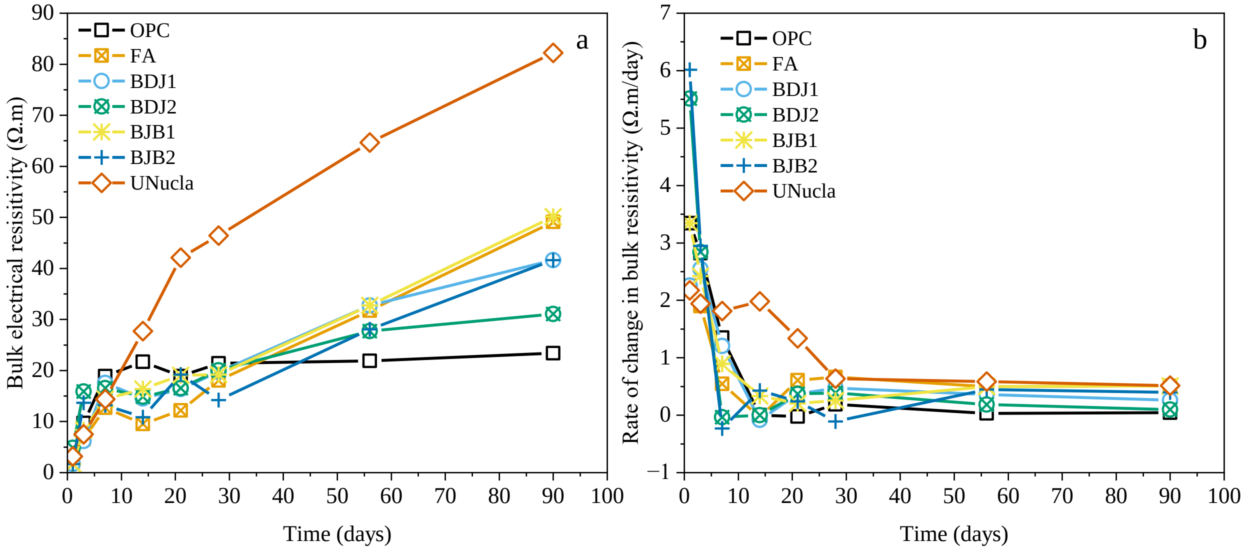

Figure 4.10 (a) Bulk electrical resistivity of OPC, FA, and LFA mortar specimen. (b) rate of change in bulk electrical resistivities.

Figure 4.11a shows the measured average surface electrical resistivity of mortar specimens and the corresponding 95% confidence interval. In general, the surface electrical resistivity results are in good agreement with the bulk resistivity results. Similar to the bulk resistivity values shown in Figure 4.10, the measured surface resistivity of the specimens increased with time in the same order, albeit with higher resistivity values. Figure 4.11b suggests that one day after casting the specimens, the surface-to-bulk electrical resistivity ratios (SR/BR) ranged from 5.7 in UNucla to 12.6 in BJB2. However, the SR/BR values dropped significantly afterward and plateaued between 2 and 3 at later ages. Other studies have reported similar SR/BR values ranging from 2 to 4 [98-100].

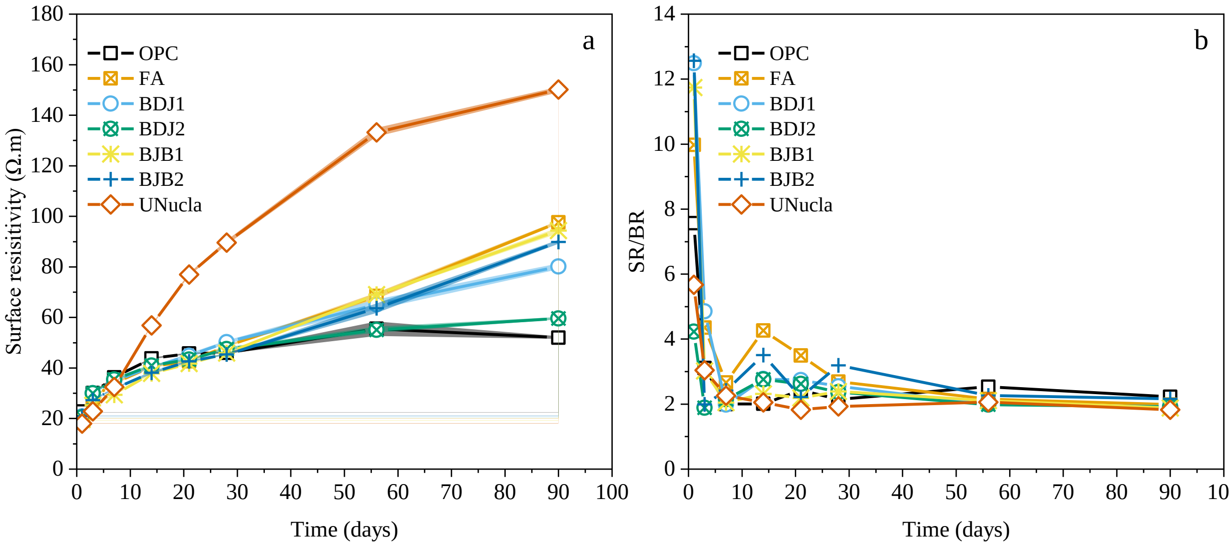

Figure 4.11 (a) Surface resistivity mortar specimen. (b) The surface-to-bulk electrical resistivity ratio over time. The shaded areas represent 95% confidence intervals.

4.7 Rapid Chloride Permeability Test Results

The RCPT is integral to concrete durability assessment because it evaluates the material's resistance to chloride ion penetration, a crucial factor in preventing reinforcement corrosion and ensuring the long-term structural integrity of concrete structures [101, 102]. High resistance to chloride ion penetration signifies reduced vulnerability to deterioration mechanisms, enhancing concrete's overall durability and extended service life.

Figure 4.12 illustrates the outcomes of the RCPT along with the qualitative zones for chloride ion penetrability as recommended by ASTM C1202 [70]. Based on the results, OPC, which recorded a total charge passed a value of 5,220 coulombs, falls in the high chloride penetrability zone. The results show that the inclusion of FA led to a substantial reduction of 359% in the total charges passed over a 56-day timeframe. Except for BDJ2, which did not significantly influence the results of the chloride permeability test, all other specimens incorporating LFA demonstrated a significant reduction in the total charge that passed compared with OPC. The most remarkable reduction was observed in UNucla, showcasing an impressive 423% reduction in total charge passed that signifies major enhancement in chloride resistance, even lower than FA by 12%. Following next, BJB1 demonstrated a 248% reduction in total charge passed compared with OPC, placing it within the low chloride ion penetrability zone. Both BJB2 and BDJ1 showed reductions of 144% and 122% in the total charge passed compared with OPC, respectively, categorizing them as mixes with moderate chloride penetrability. Finally, BDJ2's slight reduction of 1% aligned it closely with the OPC.

The rise in concrete resistivity and the reduction in the transferred charge in concrete incorporating LFAs can be attributed to two primary factors. One aspect involves alterations in the concrete's pore structure, leading to the formation of smaller pores and decreased porosity [34, 103]. The other aspect relates to the decrease in the ionic strength and conductivity of the pore solution within the concrete due to the pozzolanic reaction triggered by the presence of fly ash. Research has revealed a direct correlation between the resistivity of the concrete and that of the pore solution, along with its overall porosity and the connectivity of the pores [103].

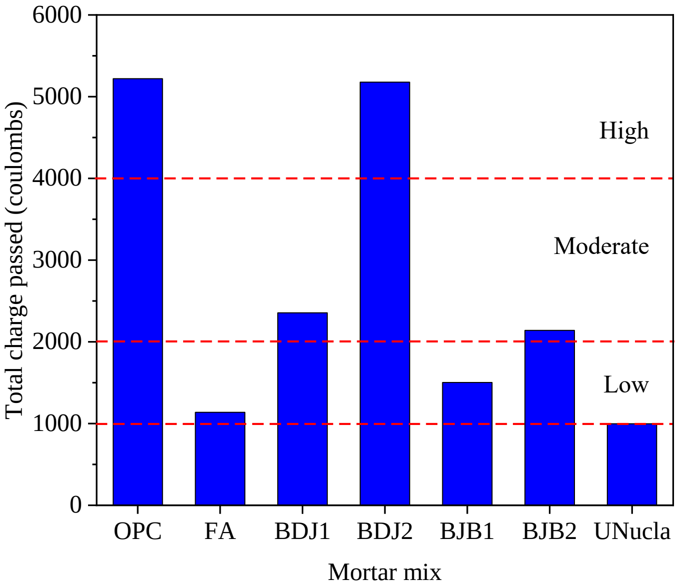

Figure 4.12 Rapid chloride permeability test results for OPC, FA, and LFA mortar specimen

4.8 Alkali-silica Reaction Expansion

ASR is a chemical reaction that occurs in concrete and can significantly affect its long-term durability [104, 105]. ASR involves the interaction between alkalis in the cement and reactive siliceous aggregates, leading to the formation of a gel-like substance. This gel can expand over time, causing cracks and damage to the concrete, which in turn compromises its structural integrity and overall durability [104, 105].

Figure 4.13 illustrates the expansion of OPC, FA, and LFA mortars over a 14-day period as part of the ASTM C1567 test. On the initial day of exposure to the NaOH solution, all samples underwent a slight expansion of less than 0.1%. Subsequently, while the expansion of FA and UNucla mortars continued to rise gradually throughout the test, the OPC specimen and the other LFA-blended specimens demonstrated a substantial acceleration in expansion rate up until day three, followed by a comparatively slower expansion rate. This indicates that it took about two to three days for a sufficient concentration of hydroxyl ions to accumulate in the OPC and other specimens containing BDJ1, BDJ2, BJB1, and BJB2 ashes to initiate ASR. By the conclusion of the testing period, the OPC specimen displayed the most extensive expansion at 0.71%, followed in descending order by BDJ2 (0.60%), BDJ1 (0.52%), BJB1 (0.51%), BJB2 (0.41%), UNucla (0.25%), and FA (0.22%).

The reduction in ASR-induced expansion resulting from the inclusion of LFAs can be attributed to several underlying factors. First, the replacement of a portion of cement with LFA, given the relatively lower reactivity of LFAs compared with cement, results in a reduction of alkalinity in the mortar's pore solution [106, 107]. This reduction, in turn, slows down the ASR process. Second, LFAs exhibited a pozzolanic characteristic that leads to the consumption of portlandite and the generation of C–S–H [95, 96]. In comparison with the OPC specimen, the additional C–S–H formed has the capacity to bind alkalis and hydroxyl ions, effectively removing them from the mortar's pore solution [108, 109]. Prior research has shown that the C–S–H produced through pozzolanic reactions tends to have a lower C/S ratio, making it more adept at absorbing alkalis that can trigger ASR [110]. Third, as indicated in Table 4.1, all LFAs exhibit significantly higher alumina content compared with OPC. A portion of alumina from LFAs can dissolve in the pore solution, promoting the pozzolanic reaction that results in the formation of calcium-Alumino-silicate-hydrate (C–A–S–H), which can ultimately suppress ASR [111]. Finally, due to the pozzolanic reaction triggered by LFAs, the microstructure of the mortars undergoes modification and becomes progressively denser over time [112]. This phenomenon can result in a reduction in the rate of alkali elements, such as sodium, penetrating from the external environment into the mortar. Consequently, this slowdown in penetration contributes to a deceleration of the ASR attack [113].

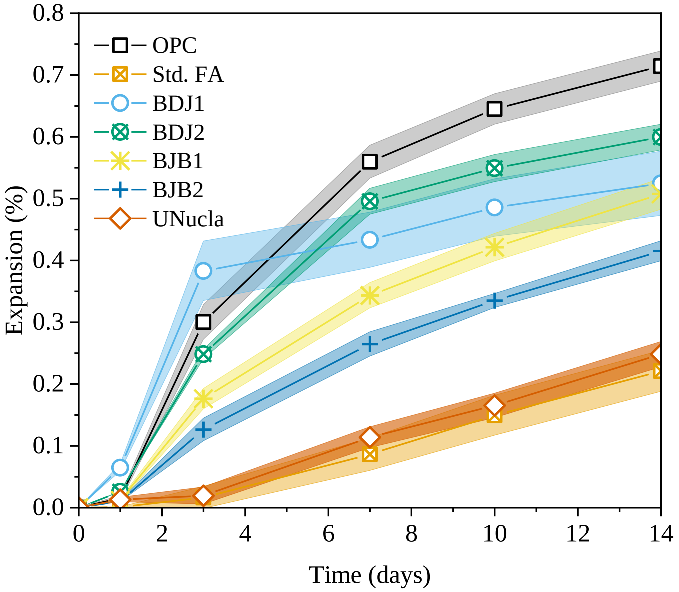

Figure 4.13 Recorded ASR-induced expansion of OPC, FA, and LFA mortar specimens. The shaded areas represent 95% confidence intervals.

Figure 4.14 presents visual indications of the degree of cracking resulting from ASR in OPC and other specimens. These observations can be effectively correlated with the specific expansion data for each individual specimen. In the case of OPC, BDJ1, and BDJ2 specimens that encountered significant expansions, there was a noticeable abundance of wide cracks spreading outward in a branching manner. Among these specimens, BDJ2, as shown in Figure 4.14d, exhibited some of the widest cracks, a few of which extended longitudinally along the mortar bar. In contrast, BJB1 and BJB2, having undergone comparatively lower expansion than OPC, displayed finer cracks that were less scattered. Remarkably, the UNucla specimen exhibited no visible signs of cracking on its surface, aligning with its minimal expansion results. On the other hand, the FA sample displayed faint traces of fine cracks on its surface, implying that the UNucla ash was more effective in suppressing ASR-induced cracking.

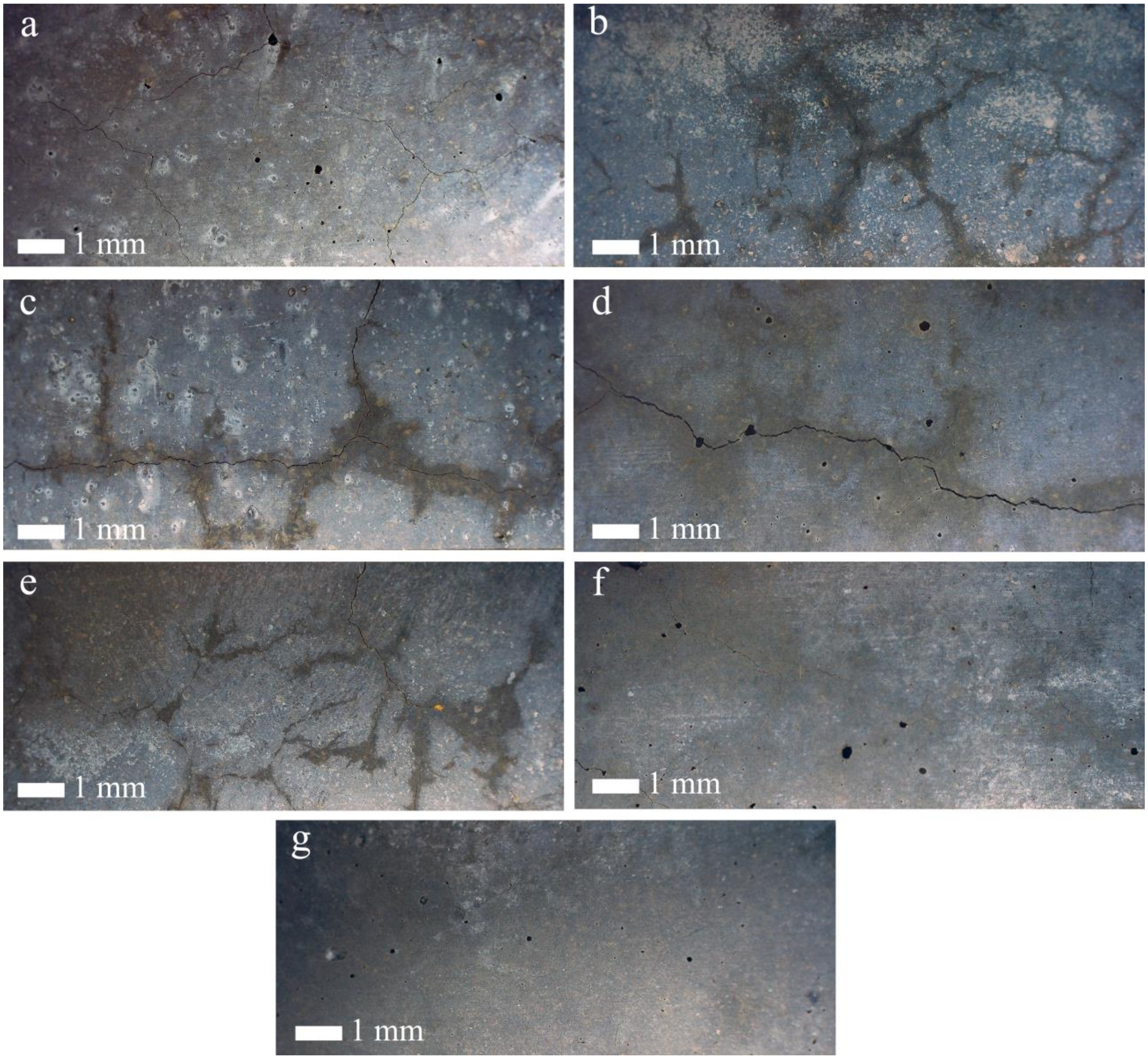

Figure 4.14 Visual inspection of ASR cracks. (a) OPC, (b) FA, (c) BDJ1, (d) BDJ2, (e) BJB1, (f) BJB2, (g) UNucla.

4.9 Absorption Rate of Water

The absorption rate of water is closely related to concrete durability because it directly influences the material's ability to resist moisture and chemical penetration, which are critical factors in maintaining its long-term structural integrity [114, 115]. A high absorption rate means that concrete can readily absorb water and potentially harmful substances, making it more vulnerable to deterioration mechanisms like freeze-thaw cycles, sulfate attack, and corrosion of embedded reinforcement [116]. In contrast, low water absorption indicates a concrete's resistance to moisture ingress and chemical penetration, contributing to its long-term durability and service life. Therefore, controlling and minimizing water absorption is crucial for ensuring concrete's durability in real-world applications. Figure 4.15 displays the results of the water absorption test conducted on 28-day mortar specimens, while Figure 4.16 illustrates the corresponding initial and secondary rates of absorption for each individual specimen. The results indicate a linear relationship between absorption and the square root of elapsed time. In Figure 4.15, it is evident that the inclusion of FA and LFAs led to a significant reduction in water absorption. Among the various specimens tested, the OPC mortar exhibited the highest water absorption of 3.53 mm; whereas, the UNucla specimen demonstrated the lowest absorption at 0.98 mm. Interestingly, the water absorption of FA closely resembled that of BJB1. Notably, both BDJ1 and BDJ2 showcased absorption rates 15.8% and 37% higher than FA, while displaying absorption rates 45.9% and 36% lower than OPC.

The initial absorption rate represents the rate at which water is initially absorbed by the concrete surface, while the secondary absorption rate represents the continued rate of water absorption after the initial absorption has taken place. The results in Figure 4.16 show that OPC exhibited the highest initial absorption rate as well as the highest secondary absorption rate, indicating a more porous structure that readily absorbed water. Conversely, the UNucla specimen demonstrated the lowest absorption rates, reflecting a denser and less porous composition. The incorporation of FA resulted in the second lowest absorption rates after UNucla, suggesting enhanced resistance to water penetration. Among the other specimens, BDJ1, BDJ2, BJB1, and BJB2 demonstrated intermediate absorption rates.

The absorption rate is directly linked to pore structure characteristics like porosity, pore size, and pore interconnectivity [117]. The diminished initial and secondary absorption rates observed in specimens containing FA and LFA imply that incorporating these materials led to the refinement of pores and likely a reduction in the porosity of the mortar specimens [21]. These findings are consistent with the results from both the RCPT and bulk electrical resistivity tests, as well as previous investigations [33, 118], suggesting that the inclusion of LFAs can reduce the absorption of harmful species and improve the durability of concrete.

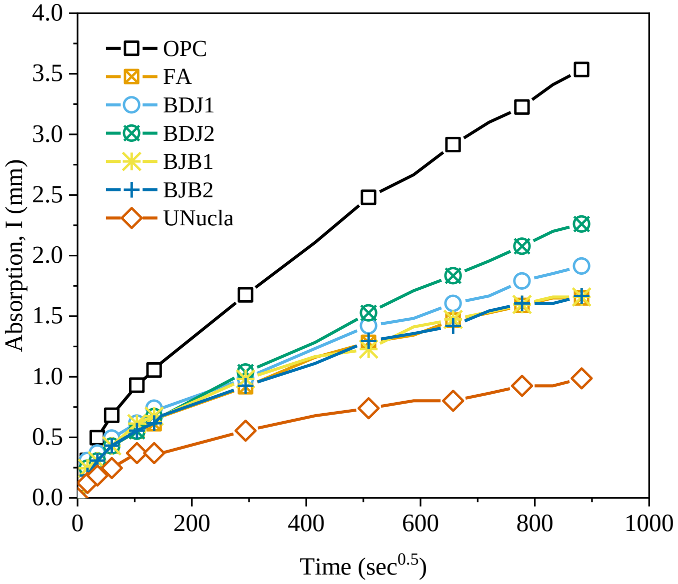

Figure 4.15 Water absorption of OPC, FA, and LFA mortar specimens

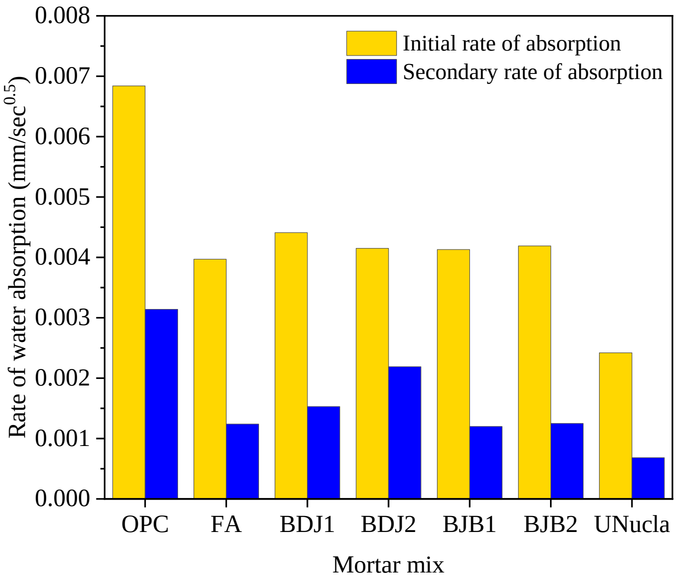

Figure 4.16 Initial and secondary rate of water absorption of OPC, FA, and LFA mortar specimens

5. DISCUSSION

5.1 Relationship Between LOI Measurements and Carbon Content

Figure 5.1 illustrates the measured LOI at different temperatures using both a furnace and TGA, along with the measured total carbon content of the LFAs. The LOI test has traditionally been employed to assess the presence of unburned carbon. According to ASTM C311 [50], the LOI is estimated by gradually heating a sample in a furnace, commencing at 110°C ± 5°C and reaching 750°C ± 50°C. The resulting weight loss within the specified temperature range, i.e., between 110°C ± 5°C and 750°C ± 50°C, is then reported as the LOI percentage. Several studies have raised concerns regarding the LOI method, suggesting a potential for overestimating unburned carbon in fly ash [75, 76, 119-121].

Figure 5.1 demonstrates that temperature and the measurement method employed for LOI can significantly influence the results. For instance, increasing the temperature from 750°C to 950°C using the furnace method resulted in an average LOI increase of 2.3%. Utilizing TGA to assess mass loss also revealed an average increase of 12% and 70% in the measured LOI at 750°C and 950°C, respectively, compared with the furnace method. Conversely, the measured total carbon contents of DJ1, JB1, and JB2 ashes were, on average, 75% lower than the measured furnace LOI at 750°C. DJ2's total carbon content was 4% higher than the furnace LOI at 750°C and 17% lower than the TGA LOI measured at the same temperature. Similarly, Nucla ash exhibited a higher total carbon content than the measured LOI at 750°C and 950°C. However, the TGA LOI at 950°C for this ash was 40% higher than the total carbon content. This overestimation in the unburned carbon content using LOI methods arises from the inclusion of various factors in the measurement, such as the mass change attributed to dehydroxylation of physically or chemically adsorbed water, which can originate from substances like portlandite, gypsum, or residual clays [74, 77]. It also includes water contained within aluminosilicates, iron minerals, and sulfates, as well as the decomposition of calcite, dolomite, and sodium bicarbonate [74, 77]. The release of other volatile organic compounds and the potential weight gain due to the oxidation of sulfide upon heating also contribute to this issue [76, 119]. As a result, it is essential to recognize that while the LOI test is a useful tool for quality control, it may not provide an exact quantification of unburned carbon in fly ash and should be interpreted with this limitation in mind.

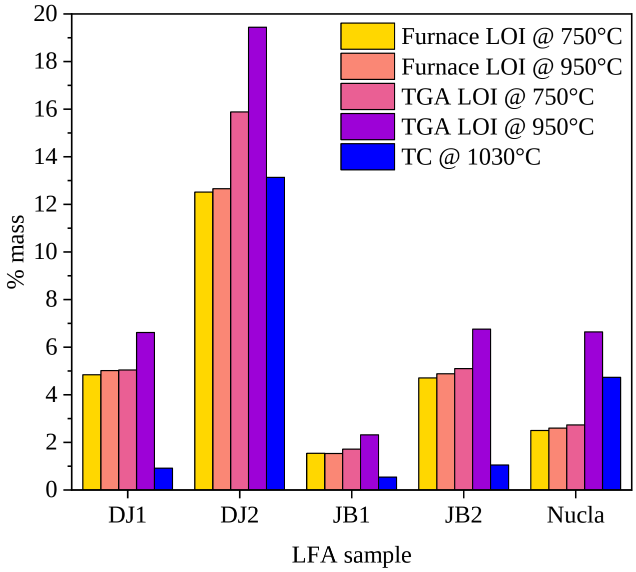

Figure 5.1 The relationship between LOI, TGA, and total carbon content

Figure 5.2 displays the relationship between furnace and TGA LOI at 750°C and 950°C, and total carbon content. The red lines in this figure represent the linear models fitted to the data. The results show strong correlations between furnace LOI at 750°C and other LOI measurements ($R^2 > 0.95$). According to the coefficients of the fitted models, the measured LOI values in the furnace model at different temperatures had an almost 1:1 relationship, while the TGA results were higher. At 750°C, the TGA LOI was, on average, 1.31 times the furnace LOI; at 950°C, the TGA LOI was, on average, 1.46 times the furnace LOI at 750°C. The increase in mass loss in TGA, especially at 950°C, can be associated with the reduction of iron and sulfur compounds at this temperature [46, 74-76].

Figure 5.2d illustrates a moderate correlation between total carbon content and furnace LOI at 750°C, with the coefficient being close to 1. Note that total carbon content encompasses both organic and inorganic carbons [73, 74]. Unburned carbon in fly ash that can be reduced through thermal processing mainly consists of organic carbon, while inorganic carbons are primarily in the form of carbonates in the ash. To separate inorganic carbon from organic carbon in fly ash, an acid treatment can be employed prior to combustion [122]. However, this process requires further processing; careful consideration is necessary when selecting the acid and its concentration and ensuring the ash is not exposed to air after acid treatment to avoid carbonation.

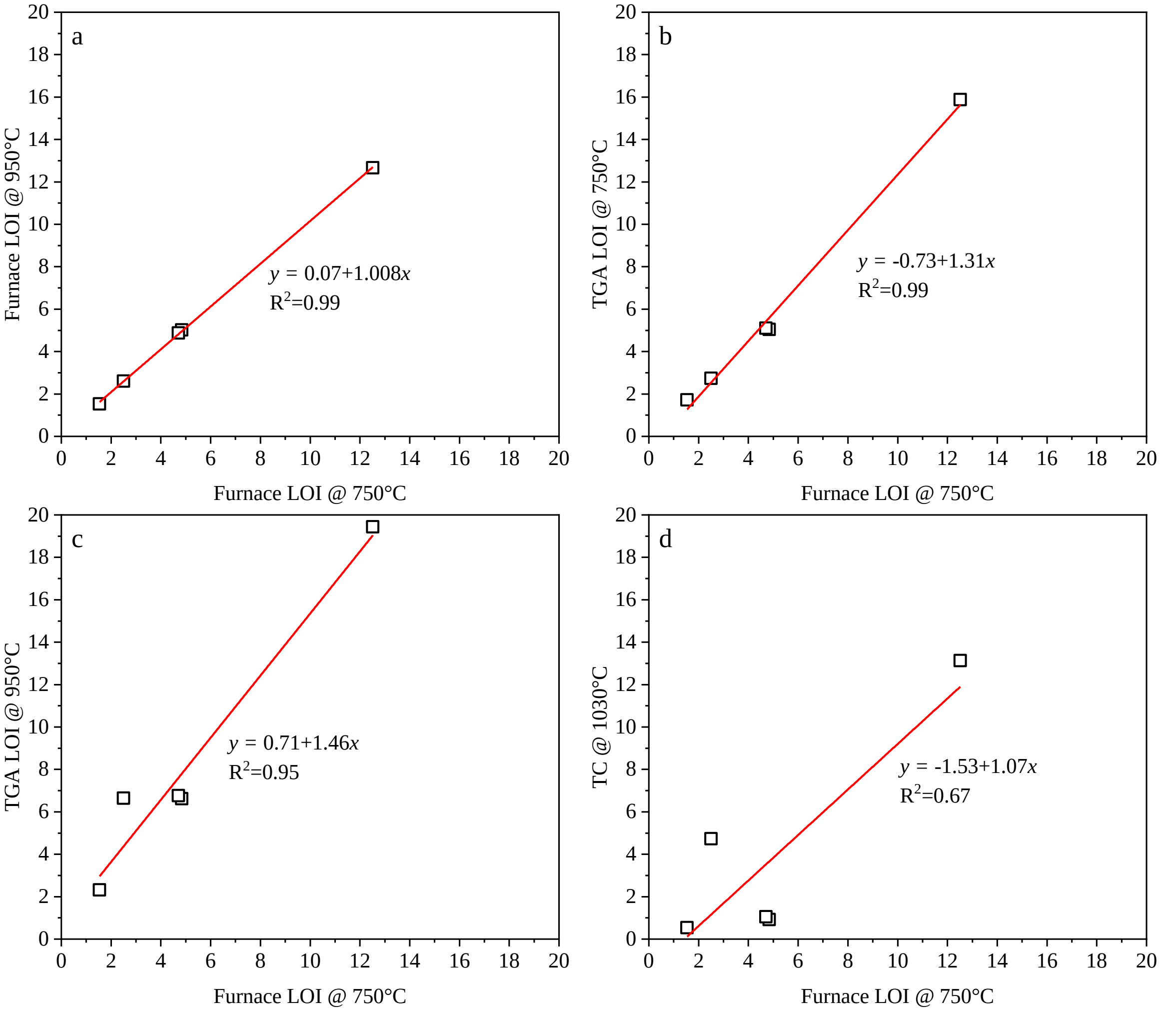

Figure 5.2 The relationship between LFA furnace LOI at 750°C (a) furnace LOI at 950°C, (b) TGA LOI at 750°C, (c) TGA LOI at 950°C, and (d) total carbon content

5.2 Relationship Between Beneficiation Temperature, LOI and LFA Reactivity

Figure 5.3 shows a strong inverse exponential relationship between thermal beneficiation temperature and furnace LOI at 750°C. The inverse exponential relationship signifies that LOI reduction is significant at higher temperatures and plateaus as the temperature continues to rise. This trend can be attributed to the decreasing availability of volatile matter to combust as the temperature surpasses a certain threshold. At temperatures above 450°C, the LOI of both DJ1 and DJ2 fell below 3%, indicating that this temperature range was effective in reducing the LOI to a desired level. However, it is essential to note that the LOI test results can be influenced by various factors. Procedural variations such as cooling time, cooling method, sample size, ignition duration, and ignition temperature can affect the LOI values obtained during testing [73, 123]. For instance, longer cooling times or variations in the ignition process may result in incomplete combustion, leading to higher LOI values [73, 123]. Therefore, it is crucial to carefully control and standardize these procedural factors to ensure accurate and reliable LOI measurements.

The LOI values of coal ash can also vary significantly depending on the type of coal. Lignite ashes typically have an LOI ranging from 0% to 5%, and sub-bituminous coal ashes have an LOI ranging from 0% to 3% [28, 119]. The widest range of variability is observed in bituminous coal ashes, with LOI values ranging from 0% to 15% [28, 119]. The wide range of initial LOI values exhibited by DJ1 and DJ2, spanning from 4.89% to 12.76%, underscores the broad applicability of the fitted models in Figure 5.3. These predictive models can provide practical guidance for optimizing the thermal beneficiation process and determining the appropriate temperature range to achieve desired LOI levels for LFAs from various sources.

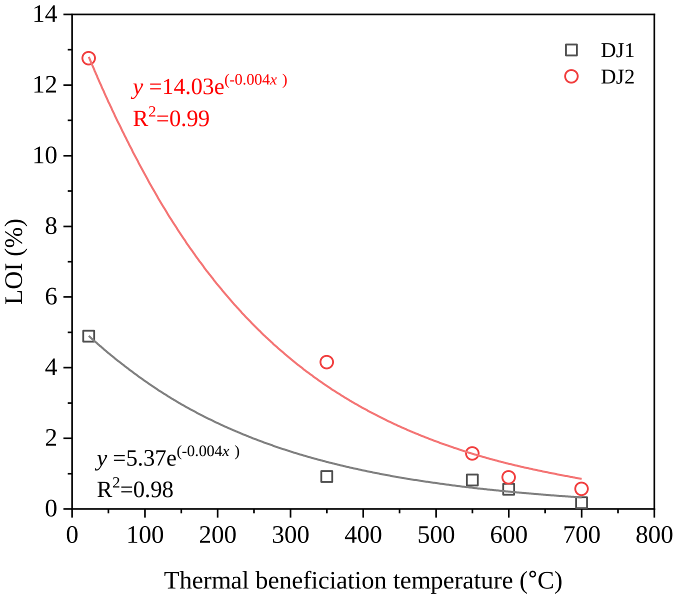

Figure 5.3 Relationship between thermal beneficiation temperature and LOI

The analysis of the relationship between thermal beneficiation temperature and the results of the modified R^3 test proved to be significant. However, since the beneficiation temperature directly affects the LOI, and LOI plays a critical role in hydration kinetics, the following discussion will focus solely on the relationship between LOI and heat release, as well as LOI and calcium hydroxide content.

Figure 14 shows that the relationship between LOI and heat release in the modified R^3 test can be modeled by a second-order non-linear quadratic equation. Notably, the specific relationship between LOI and heat release in LFA hydration may vary depending on the composition and characteristics of the LFA used.

The general trend observed in Figure 5.4 suggests that reducing the LOI can increase the reactivity of fly ash, as indicated by the increase in heat release. However, the concave-down shape of the fitted line suggests the existence of an inflection point at about 2% LOI for DJ1 and 4% LOI in DJ2. This inflection point suggests that any further reduction in LOI below these thresholds may not necessarily impact the hydration kinetics significantly. Note that LOI test results from a muffle furnace may overestimate the amount of organic carbon present in fly ash due to possible reactions, such as the calcination of inorganic carbonates, desorption of physically and chemically bound water, and oxidation of sulfur and iron minerals [73]. Therefore, it can be hypothesized that excessively heating LFA to reduce its LOI, particularly below 1%, may affect the chemical properties of the ash, thereby influencing the heat release. The observed slight decrease in heat release below the inflection point in Figure 5.4 further supports this hypothesis.

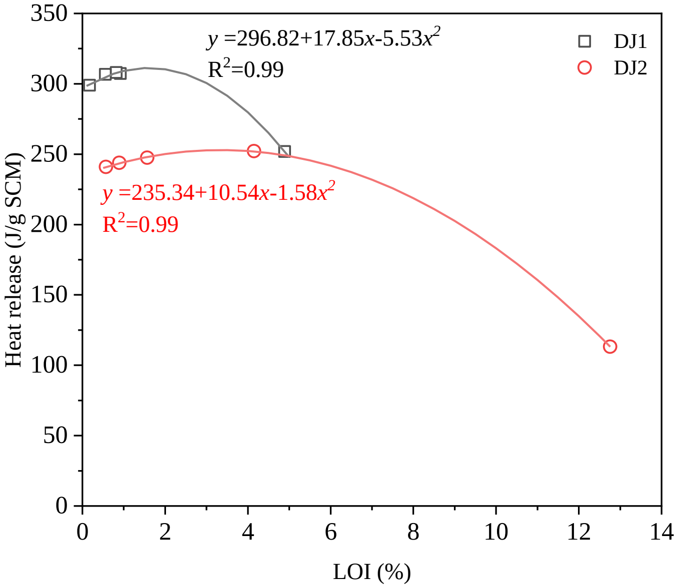

Figure 5.4 Relationship between LOI and heat release

Figure 5.5 shows a strong non-linear inverse relationship between LOI and calcium hydroxide consumption. This finding indicates that reducing the LOI of LFA increases its reactivity to consume more calcium hydroxide, mainly due to a decrease in the organic contents that interfere with pozzolanic reactions. The unburned carbon, for example, can physically hinder the contact between the pozzolanic components of the ash and calcium hydroxide, thereby limiting their reaction [124]. Carbon particles can also act as a barrier that slows down the diffusion of calcium hydroxide into the ash particles, further impeding the pozzolanic reaction [119]. Therefore, reducing the unburned carbon content can increase the pozzolanic activity of LFA. However, it is important to note that, as discussed earlier, the majority of LOI in most of the ashes in this study is attributed to the dehydroxylation of other compounds, such as lime and carbonates. The power functions fitted in Figure 5.5 exhibit a negative exponent power, indicating that the correlation between LOI and calcium hydroxide consumption follows an asymptotic pattern. As the LOI of the LFAs increases toward its maximum value, the amount of calcium hydroxide consumed tends to approach the lowest possible values of 12.83 g/100 g SCM for DJ1 and 23.1 g/100 g SCM for DJ2.

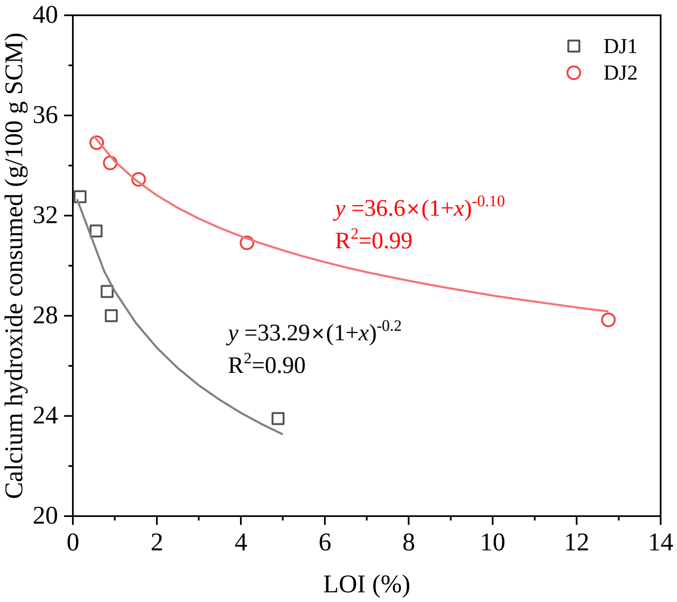

Figure 5.5 Relationship between LOI and consumed calcium hydroxide content

5.3 Relationship Between Specific Surface Area and LFA Reactivity Parameters

Figures 5.6 and 5.7 demonstrate a strong correlation between the fineness of LFA and heat release, and fineness of LFA and $Ca(OH)_2$ consumption, respectively. Other studies have also reported correlations between fineness and various properties, including LOI [46], mechanical properties [125, 126], microstructure characteristics [126], cement hydration [127], and durability properties [128, 129].
The results indicate that increasing the fineness of LFA, which is directly related to the grinding time, can lead to enhanced reactivity of LFA as measured in the modified-R^3 test. While the correlation between specific surface area and heat release shows a linear fit with low variability, the relationship between specific surface area and calcium hydroxide consumption exhibits a wider spread. Although increasing fineness is typically associated with increased reactivity, enhanced packing effect, and nucleation effect [130], the chemical composition of LFA plays a more significant role, and fineness alone cannot solely predict the reactivity of LFA. This is particularly noteworthy because a recent study on size-fractionated unconventional fly ashes revealed that as the size fractions became coarser, the CaO contents decreased and SiO_2 contents increased [131]. Coarser fractions also exhibited a higher presence of impurities and unburnt carbon particles, while finer fractions contained limited amounts of such particles [131]. Further research on the role of fineness in cement hydration kinetics would be valuable, especially if the chemical composition can be controlled.

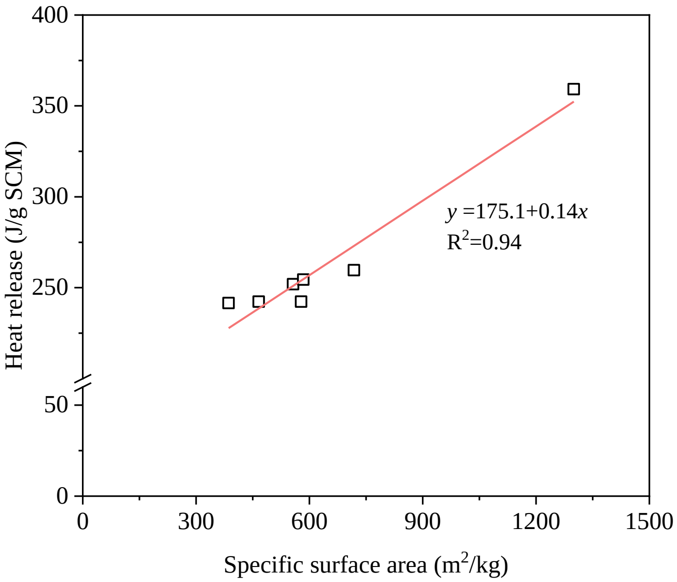

Figure 5.6 Relationship between specific surface area and heat release

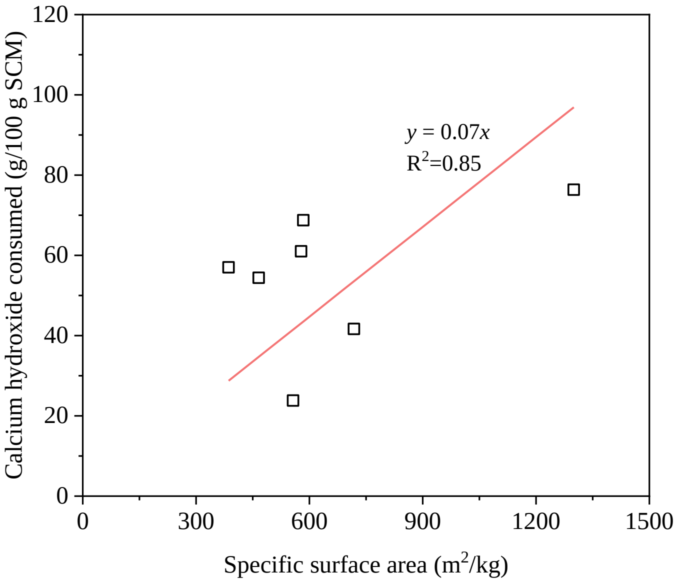

Figure 5.7 Relationship between specific surface area and consumed calcium hydroxide content

5.4 Relationship Between Ca(OH)2 Consumption, Heat Release, DoR, and SAI

Figure 5.8 presents the correlation matrix involving 10-day consumed calcium hydroxide, 10-day heat release, predicted DoR, and the strength activity indices at 28 and 90 days. The results show that 10-day $Ca(OH)_2$ consumption has a positive correlation of 0.62 with 10-day heat release, indicating that higher $Ca(OH)_2$ consumption leads to increased heat release. Additionally, a moderate positive correlation of 0.56 exists between 10-day $Ca(OH)_2$ consumption and DoR, suggesting that materials with higher reactivity tend to consume more $Ca(OH)_2$. However, the correlation between 10-day $Ca(OH)_2$ consumption and SAI at 28 and 90 days is relatively weak. This was expected due to the slow strength development in paste specimens containing LFAs, making early $Ca(OH)_2$ consumption less reliable as an indicator to predict strength development. Other studies have shown a negative correlation between the calcium hydroxide content and seven-day lime strength test results [132]. The lime strength test is similar to the R^3 test in terms of sample preparation, with the exception that K_2SO_4 is also added to the system, and the samples are initially cured for 24 hours followed by oven curing at 40°C for 48 hours and then placed inside distilled water for seven days [133].

Figure 5.8 shows a strong positive correlation of 0.98 exists between 10-day heat release and DoR, indicating that materials with higher reactivity levels exhibit greater heat release. In terms of SAI, 10-day heat release shows a moderate positive correlation of 0.5 with 28-day SAI and 0.71 with 90-day SAI, suggesting that higher heat release is associated with increased strength development over time, particularly at the later age. Similar findings have been reported regarding the correlation between heat release and lime strength tests [132]. The DoR demonstrates a moderate positive correlation of 0.52 with 28-day SAI and 0.68 with 90-day SAI, indicating that materials with higher reactivity also tend to exhibit greater strength development at the later stage (90 days). The 28-day and 90-day SAI exhibit a significant positive correlation of 0.92, indicating a strong association between strength measurements at these two specific time points. This correlation underscores the fundamental mechanism of strength enhancement over time.

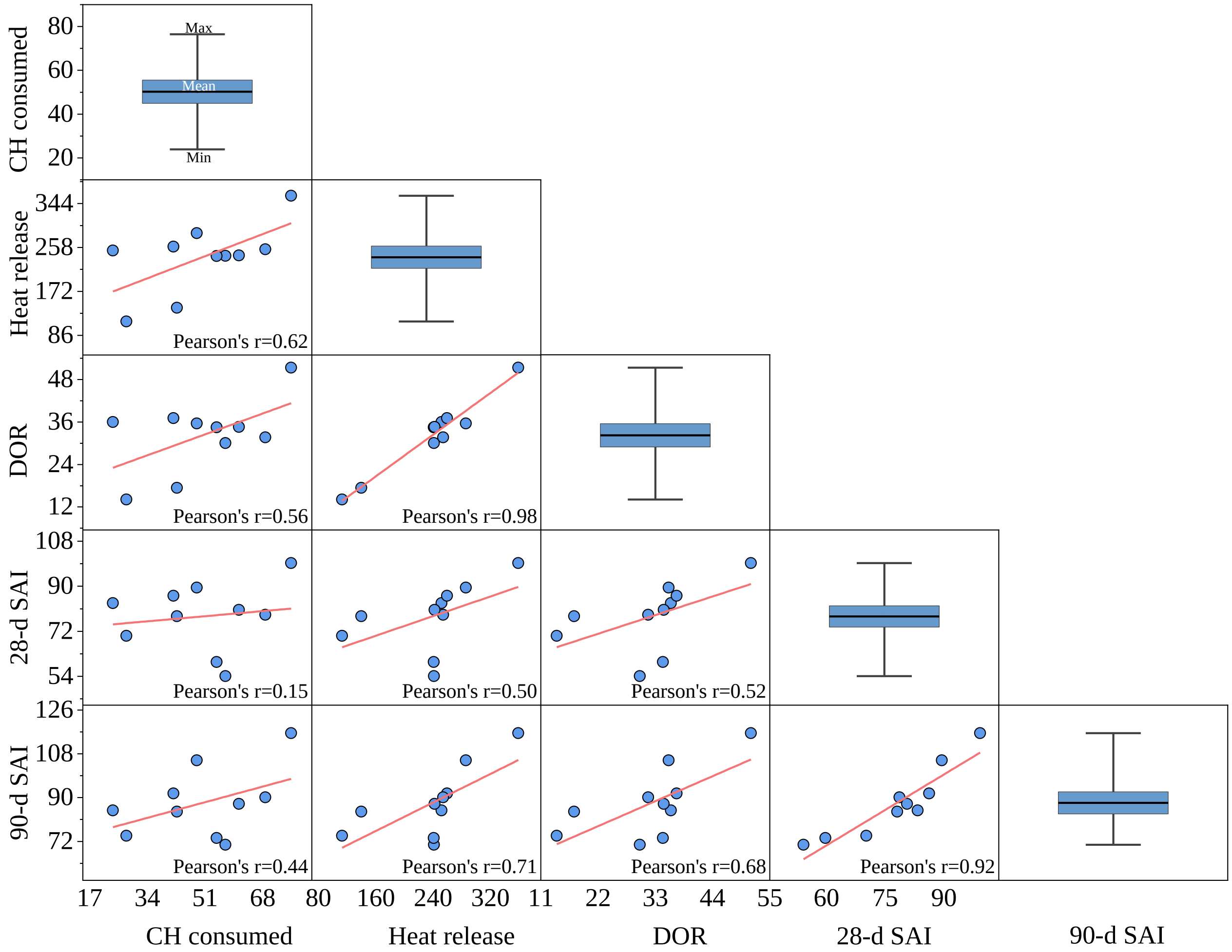

Figure 5.8 The correlation between different measures of reactivity and SAI

5.5 Quantifying the Efficacy of Thermo-mechanical Beneficiation

The heat release and consumed $Ca(OH)_2$ results shown in Figures 4.5 and 4.6 show a wide variation among LFAs tested in this study. It is crucial to emphasize that even commercially available SCMs meeting the ASTM standard requirements can exhibit significant deviations in both heat release and $Ca(OH)_2$ consumption. For instance, Suraneni et al. [134] conducted a study on 21 commercially graded fly ashes, 11 silica fumes, and 9 slags using a modified R^3 test, which revealed a wide range of results for the consumption of calcium hydroxide and cumulative heat release. Fly ashes, most specifically, demonstrated consumption levels of calcium hydroxide ranging from 43 to 81 g/100 g SCM, and cumulative heat release levels between 194 and 353 J/g SCM.

Figure 5.9 displays the relationship between consumed $Ca(OH)_2$ and the heat release of LFAs, as well as the path that the beneficiation method took, which is represented by an arrow for each LFA. Various standard SCMs tested by Suraneni et al. [134] are superimposed on this plot for comparison purposes. The classification depicted in Figure 19 categorizes fly ash as “pozzolanic-less reactive,” slag as “latent hydraulic-more reactive,” and silica fume as “pozzolanic-more reactive.” These SCMs and proposed classifications are included here only for comparison. For a more comprehensive discussion, readers are encouraged to refer to the study by Suraneni et al. [134]. By comparing the consumption of calcium hydroxide and cumulative heat release of LFAs with the reported ranges for other traditional SCMs, it becomes apparent that the unbeneficiated samples obtained from JB and Nucla power plants can be categorized as pozzolanic-less reactive. DJ2 falls within the region of inert materials. DJ1 lies outside the pozzolanic range, possibly due to the presence of excessive lime in this sample, and falls between the inert, pozzolanic, and latent hydraulic regions. The results indicate that after the samples underwent the beneficiation process, all LFAs fell within the region of pozzolanic-less reactive materials, exhibiting similar values for heat release and consumed calcium hydroxide compared with reference fly ashes. It is crucial to highlight that even SCMs conforming to ASTM standards exhibit a considerable range of differences in their pozzolanic characteristics. This variability is an inherent attribute shared by all SCMs, and the LFAs assessed in this research demonstrate the same pattern.

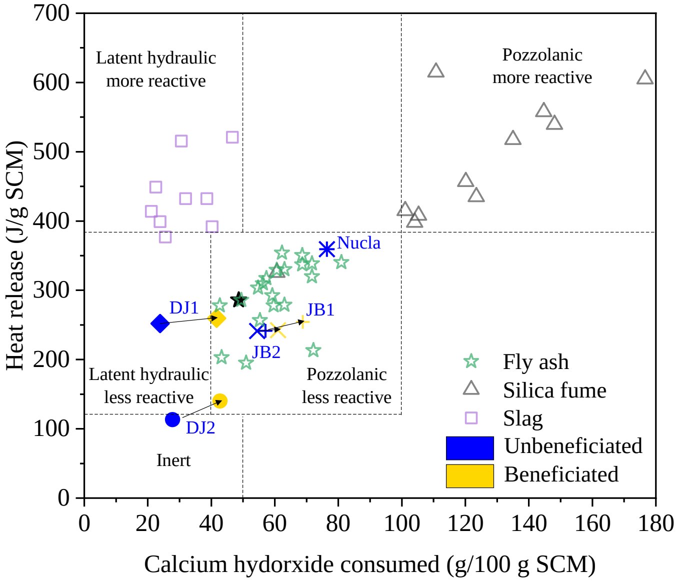

Figure 5.9 Comparison of calcium hydroxide consumption and heat release of unbeneficiated and beneficiated LFAs with conventional SCMs adopted from ref. [60]

When comparing the DoR values in Figure 4.7 with the classifications shown in Figure 5.9, it becomes evident that there may be some inconsistencies because DoR only considers heat release. For example, while unbeneficiated DJ1 is not classified as a pozzolanic material according to Figure 19, it exhibits a higher DoR than JB2 and a similar DoR to the reference fly ash. This contradiction arises from the fact that the DoR method solely relies on heat release to determine reactivity, whereas the R^3 results also consider the extent of $Ca(OH)_2$ consumption as a factor influencing reactivity. Various methods have been proposed to use the R^3 test result for calculating the degree of reactivity [135, 136]. However, these methods usually require performing additional tests on paste samples and consider the ratio of heat release [or $Ca(OH)_2$ consumption] in the paste system to that of the R^3 test as the degree of reactivity. When comparing the efficacy of a beneficiation method on various materials, one simple approach could be to determine the magnitude and direction of the position vector between pre- and post-beneficiation points in a $Ca(OH)_2$-heat release space. Mathematically, the magnitude of this beneficiation vector $\|\mathbf{v_b}\|$ can be calculated using Eq. (5):

$$\|\mathbf{V_b}\| = \sqrt{\Delta CH^2 + \Delta Q^2} \tag{5}$$

where ΔCH and ΔQ are the differences in consumed $Ca(OH)_2$ and heat release before and after beneficiation, respectively. The direction of the vector $\mathbf{v_b}$ can be defined by the horizontal angle θ given by:

$$\theta = \tan^{-1}\frac{\Delta Q}{\Delta CH} \tag{6}$$

If θ is less than 45°, then the beneficiation shifts the LFA to the region where the beneficiated LFA consumes more $Ca(OH)_2$ than it releases heat. On the other hand, if θ is greater than 45°, the beneficiation results in a shift in LFA to the region where it produces more heat than it consumes $Ca(OH)_2$. The magnitude of beneficiation vectors and their directions for the four beneficiated LFAs are given in Table 5.1. According to $\|\mathbf{v_b}\|$ values, the beneficiation process employed in this study had the greatest impact on samples located outside the pozzolanic region. DJ2 and DJ1, which were initially positioned outside the pozzolanic region according to the classification depicted in Figure 5.9, had the first and second highest $\|\mathbf{v_b}\|$ values. Based on the values of angle θ in Table 5.1, we concluded that the thermo-mechanical beneficiation does not affect the LFAs in the same way. For example, in DJ1 and JB2, θ is less than 45°, while in DJ2 and JB1, θ is greater than 45°. The authors suspect that pre-exposure to lime, moisture, and other contaminants in the landfills plays a critical role in determining the magnitude and direction of the beneficiation process. However, since this is beyond the scope of this study, further research is needed to determine the underlying factors that contribute to the path the beneficiation process takes.

Table 5.1 The influence of thermo-mechanical beneficiation on consumed $Ca(OH)_2$ and heat release

LFA source	ΔCH (g CH/100 g SCM)	ΔQ (J/g SCM)	ΔQ/ΔCH (100 J/ g CH)	θ (°)	$\|\mathbf{v_b}\|$
DJ1	17.8	7.7	0.44	23.51	19.42
DJ2	14.9	26.8	1.80	60.93	30.68
JB1	11.7	12.9	1.10	47.68	17.45
JB2	6.6	1.1	0.16	9.13	6.68

6. CONCLUSION

This study investigated how thermo-mechanical beneficiation affects the physiochemical characteristics, reactivity, and performance of landfilled fly ashes obtained from two U.S. power plants in Wyoming and Colorado. The results highlighted a significant impact of thermo-mechanical beneficiation on the physiochemical properties of LFAs, leading to reduced carbon content and increased fineness. X-ray diffraction analysis revealed minimal changes in the mineral composition of LFAs post-beneficiation. Reactivity assessments, including strength activity index and modified R^3 tests, indicated consistent improvements in LFAs after beneficiation.

The unbeneficiated LFAs exhibited varying SAI levels, with only DJ1 and Nucla LFAs meeting the minimum requirement of 75% at 28 days. Beneficiation consistently raised the SAI of all LFAs, surpassing the 75% threshold. Additionally, beneficiation increased heat release and calcium hydroxide consumption, signifying enhanced pozzolanic reactivity. The reactivity analysis classified LFAs into silico-aluminious and silicious materials, with moderate degree of reactivity (DoR) variations among LFAs, showing an average increase of 8.1% after beneficiation. However, disparities emerged when comparing DoR values with the classification based on heat release, emphasizing the limitations of individual test methods.

In conclusion, key insights from this study include:

- Higher temperatures led to a significant reduction in LOI, plateauing above 450°C.
- The relationship between LOI and heat release suggested that reducing LOI could enhance fly ash reactivity, but an inflection point indicated diminishing returns below certain LOI thresholds.
- Excessive heating to reduce LOI below 1% could impact ash chemical properties and influence heat release.
- Fineness (specific surface area) correlated with heat release and calcium hydroxide consumption, emphasizing its importance for enhanced reactivity. However, fineness alone could not predict reactivity, as the chemical composition also played a significant role.
- Associations were found between calcium hydroxide consumption, heat release, and strength activity indices at different time points, indicating that higher calcium hydroxide consumption and heat release correlated with increased reactivity and strength development over time, particularly in later stages.
- Unbeneficiated LFAs did not match the strength of OPC at both 28 and 90 days. However, certain unbeneficiated LFAs, such as UNucla, showed competitive strength levels, even surpassing OPC at 28 days. Beneficiated LFAs exhibited promising performance, with all LFA mortars achieving strength levels comparable to or even exceeding OPC and FA ash at both 28 and 90 days.
- Initially lower than OPC, LFAs' electrical resistivity evolved over time, surpassing OPC after 56 days, suggesting evolving microstructural changes. Notably, LFAs like UNucla exhibited superior resistivity than FA, indicating improved microstructure.
- While OPC exhibited elevated chloride penetrability, most LFAs demonstrated a marked reduction in chloride ingress. UNucla notably surpassed FA, showcasing enhanced resistance against chloride penetration. BDJ1 and BJB1 further exhibited substantial decreases in charge passed, highlighting their potential to enhance durability by reducing chloride ingress.
- All LFAs effectively suppressed ASR-induced expansion due to factors like reduced pore solution alkalinity, pozzolanic reaction products, and altered microstructure.
- Incorporating LFAs led to reduced water absorption rates, indicating enhanced durability potential and improved water penetration resistance.

While this study provides valuable insights, further research could explore LFAs' long-term performance and environmental implications in concrete production. The site-specific nature of LFAs emphasizes the need for tailored approaches to effectively harness their potential. This investigation underscores the potential of thermomechanically beneficiated LFAs as sustainable alternatives to conventional fly ash, offering environmentally conscious strategies for achieving durable and eco-friendly construction practices.

7. REFERENCES

1. Juenger, M.C., Snellings, R., and Bernal, S.A., *Supplementary Cementitious Materials: New Sources, Characterization, and Performance Insights.* Cement and Concrete Research, 2019. **122**: p. 257-273.
2. Skibsted, J. and Snellings, R., *Reactivity of Supplementary Cementitious Materials (Scms) in Cement Blends.* Cement and Concrete Research, 2019. **124**: p. 105799.
3. von Greve-Dierfeld, S., Lothenbach, B., Vollpracht, A., Wu, B., Huet, B., Andrade, C., Medina, C., Thiel, C., Gruyaert, E., and Vanoutrive, H., *Understanding the Carbonation of Concrete with Supplementary Cementitious Materials: A Critical Review by Rilem Tc 281-Ccc.* Materials and structures, 2020. **53**(6): p. 136.
4. Elahi, M.M.A., Shearer, C.R., Reza, A.N.R., Saha, A.K., Khan, M.N.N., Hossain, M.M., and Sarker, P.K., *Improving the Sulfate Attack Resistance of Concrete by Using Supplementary Cementitious Materials (Scms): A Review.* Construction and Building Materials, 2021. **281**: p. 122628.
5. Rahla, K.M., Mateus, R., and Bragança, L., *Comparative Sustainability Assessment of Binary Blended Concretes Using Supplementary Cementitious Materials (Scms) and Ordinary Portland Cement (Opc).* Journal of Cleaner Production, 2019. **220**: p. 445-459.
6. Atiş, C.D., *Strength Properties of High-Volume Fly Ash Roller Compacted and Workable Concrete, and Influence of Curing Condition.* Cement and Concrete research, 2005. **35**(6): p. 1112-1121.
7. Kumar, M., Sinha, A.K., and Kujur, J., *Mechanical and Durability Studies on High-Volume Fly-Ash Concrete.* Structural Concrete, 2021. **22**: p. E1036-E1049.
8. Singh, L., Ali, D., Tyagi, I., Sharma, U., Singh, R., and Hou, P., *Durability Studies of Nano-Engineered Fly Ash Concrete.* Construction and Building Materials, 2019. **194**: p. 205-215.
9. De Maeijer, P.K., Craeye, B., Snellings, R., Kazemi-Kamyab, H., Loots, M., Janssens, K., and Nuyts, G., *Effect of Ultra-Fine Fly Ash on Concrete Performance and Durability.* Construction and Building Materials, 2020. **263**: p. 120493.
10. Wang, T., Ishida, T., Gu, R., and Luan, Y., *Experimental Investigation of Pozzolanic Reaction and Curing Temperature-Dependence of Low-Calcium Fly Ash in Cement System and Ca-Si-Al Element Distribution of Fly Ash-Blended Cement Paste.* Construction and Building Materials, 2021. **267**: p. 121012.
11. Li, Y., Wu, B., and Wang, R., *Critical Review and Gap Analysis on the Use of High-Volume Fly Ash as a Substitute Constituent in Concrete.* Construction and Building Materials, 2022. **341**: p. 127889.
12. du Toit, G., van der Merwe, E.M., Kruger, R.A., McDonald, J.M., and Kearsley, E.P., *Characterisation of the Hydration Products of a Chemically and Mechanically Activated High Coal Fly Ash Hybrid Cement.* Minerals, 2022. **12**(2): p. 157.
13. Golewski, G.L., *The Role of Pozzolanic Activity of Siliceous Fly Ash in the Formation of the Structure of Sustainable Cementitious Composites.* Sustainable Chemistry, 2022. **3**(4): p. 520-534.
14. Xie, S., Yang, Q., Wang, Q., Zhou, H., Bartocci, P., and Fantozzi, F., *Coal Power Decarbonization Via Biomass Co-Firing with Carbon Capture and Storage: Tradeoff between Exergy Loss and Ghg Reduction.* Energy Conversion and Management, 2023. **288**: p. 117155.
15. Song, F., Mehedi, H., Liang, C., Meng, J., Chen, Z., and Shi, F., *Review of Transition Paths for Coal-Fired Power Plants.* Global Energy Interconnection, 2021. **4**(4): p. 354-370.
16. Asif, Z., Chen, Z., Wang, H., and Zhu, Y., *Update on Air Pollution Control Strategies for Coal-Fired Power Plants.* Clean Technologies and Environmental Policy, 2022. **24**(8): p. 2329-2347.

17. US Energy Information Administration (EIA). *Preliminary Monthly Electric Generator Inventory (Based on Form Eia-860m as a Supplmenet Form to Form Eia-860)*. 2019; Available from: https://www.eia.gov/electricity/data/eia860m/,2019.
18. NPCCA. *Fly Ash Trends Downward*. 2017; Available from: https://precast.org/2017/03/fly-ash-trends-downward/.
19. Ohenoja, K., Pesonen, J., Yliniemi, J., and Illikainen, M., *Utilization of Fly Ashes from Fluidized Bed Combustion: A Review.* Sustainability, 2020. **12**(7): p. 2988.
20. Muthusamy, K., Rasid, M.H., Jokhio, G.A., Budiea, A.M.A., Hussin, M.W., and Mirza, J., *Coal Bottom Ash as Sand Replacement in Concrete: A Review.* Construction and Building Materials, 2020. **236**: p. 117507.
21. Zahedi, M. and Rajabipour, F., *Fluidized Bed Combustion (Fbc) Fly Ash and Its Performance in Concrete.* ACI Materials Journal, 2019. **116**(4): p. 163-172.
22. Yoon, J., Jafari, K., Tokpatayeva, R., Peethamparan, S., Olek, J., and Rajabipour, F., *Characterization and Quantification of the Pozzolanic Reactivity of Natural and Non-Conventional Pozzolans.* Cement and Concrete Composites, 2022. **133**: p. 104708.
23. Kaladharan, G. and Rajabipour, F., *Evaluation and Beneficiation of High Sulfur and High Alkali Fly Ashes for Use as Supplementary Cementitious Materials in Concrete.* Construction and Building Materials, 2022. **339**: p. 127672.
24. Diaz-Loya, I., Juenger, M., Seraj, S., and Minkara, R., *Extending Supplementary Cementitious Material Resources: Reclaimed and Remediated Fly Ash and Natural Pozzolans.* Cement and concrete composites, 2019. **101**: p. 44-51.
25. Wang, Y., Burris, L., Hooton, R.D., Shearer, C.R., and Suraneni, P., *Effects of Unconventional Fly Ashes on Cementitious Paste Properties.* Cement and Concrete Composites, 2022. **125**: p. 104291.
26. ASTM C618-23, *Standard Specification for Coal Fly Ash and Raw or Calcined Natural Pozzolan for Use in Concrete*. 2023, ASTM International: West Conshohocken, PA.
27. AASHTO M 295 *Standard Specification for Coal Fly Ash and Raw or Calcined Natural Pozzolan for Use in Concrete*. 2011, American Association of State Highway and Transportation Officials
28. Heidrich, C., Feuerborn, H.-J., and Weir, A. *Coal Combustion Products: A Global Perspective*. in *World of coal ash conference*. 2013.
29. Balachandra, A.M., Abdol, N., Darsanasiri, A., Zhu, K., Soroushian, P., and Mason, H.E., *Landfilled Coal Ash for Carbon Dioxide Capture and Its Potential as a Geopolymer Binder for Hazardous Waste Remediation.* Journal of Environmental Chemical Engineering, 2021. **9**(4): p. 105385.
30. Robl, T., Oberlink, A., and Jones, R., *Coal Combustion Products (Ccps): Characteristics, Utilization and Beneficiation*. 2017: Woodhead Publishing.
31. ASTM C618-22, *Standard Specification for Coal Fly Ash and Raw or Calcined Natural Pozzolan for Use in Concrete*. 2022, ASTM International: West Conshohocken, PA.
32. Al-Shmaisani, S., Kalina, R.D., Ferron, R.D., and Juenger, M.C., *Evaluation of Beneficiated and Reclaimed Fly Ashes in Concrete.* ACI Materials Journal, 2019. **116**(4): p. 79-87.
33. McCarthy, M., Zheng, L., Dhir, R., and Tella, G., *Dry-Processing of Long-Term Wet-Stored Fly Ash for Use as an Addition in Concrete.* Cement and Concrete Composites, 2018. **92**: p. 205-215.
34. Rajabipour, F., Zahedi, M., and Kaladharan, G., *Evaluating the Performance and Feasibility of Using Recovered Fly Ash and Fluidized Bed Combustion (Fbc) Fly Ash as Concrete Pozzolan.* ACI Concrete Research Council, Final Report, 2020.
35. MICHAL, A. and MAREK, Z., *Frost Salt Scaling Resistance of Concrete Containing Cfbc Fly Ash.* Materials and Structures, 2008. **41**(5): p. 33-42.
36. Sutter, L.L., Hooton, R.D., and Schlorholtz, S., *Methods for Evaluating Fly Ash for Use in Highway Concrete*. Vol. 749. 2013: Transportation Research Board.

37. Kim, J.-K., Cho, H.-C., and Kim, S.-C., *Removal of Unburned Carbon from Coal Fly Ash Using a Pneumatic Triboelectrostatic Separator.* Journal of Environmental Science and Health, Part A, 2001. **36**(9): p. 1709-1724.
38. Bittner, J.D. and Gasiorowski, S.A. *Sti's Six Years of Commercial Experiences in Electrostatic Beneficiation of Fly Ash*. in *2001 International Ash Utilization Symposium. Center for Applied Energy Research, Uniersity of Kentucky Paper*. 2001.
39. Carroll, R.A. *Coal Combustion Products in the United Kingdom and the Potential of Stockpile Ash*. in *Proceedings of the Word of Coal Ash Conference, Nashville, TN, USA*. 2015.
40. Hurt, R.H. and Gibbins, J.R., *Residual Carbon from Pulverized Coal Fired Boilers: 1. Size Distribution and Combustion Reactivity.* Fuel, 1995. **74**(4): p. 471-480.
41. Hurt, R.H., Davis, K.A., Yang, N.Y., Headley, T.J., and Mitchell, G.D., *Residual Carbon from Pulverized-Coal-Fired Boilers. 2. Morphology and Physicochemical Properties.* Fuel, 1995. **74**(9): p. 1297-1306.
42. Dindarloo, S.R. and Hower, J.C., *Prediction of the Unburned Carbon Content of Fly Ash in Coal-Fired Power Plants.* Coal Combustion and Gasification Products, 2015. **7**(3): p. 19-29.
43. Kaladharan, G., Gholizadeh-Vayghan, A., and Rajabipour, F., *Review, Sampling, and Evaluation of Landfilled Fly Ash.* ACI Mater J, 2019. **116**: p. 113-122.
44. Nowak, B., Pessl, A., Aschenbrenner, P., Szentannai, P., Mattenberger, H., Rechberger, H., Hermann, L., and Winter, F., *Heavy Metal Removal from Municipal Solid Waste Fly Ash by Chlorination and Thermal Treatment.* Journal of Hazardous Materials, 2010. **179**(1-3): p. 323-331.
45. Mucsi, G., *Mechanical Activation of Power Station Fly Ash by Grinding–a Review.* ÉPÍTŐANYAG, 2016. **68**(2): p. 56-61.
46. Wang, Y., Acarturk, B.C., Burris, L., Hooton, R.D., Shearer, C.R., and Suraneni, P., *Physicochemical Characterization of Unconventional Fly Ashes.* Fuel, 2022. **316**: p. 123318.
47. Kuinkel, M.S., Zhang, C., Liu, P., Demirkesen, S., and Ksaibati, K., *Suitability Study of Using Uavs to Estimate Landfilled Fly Ash Stockpile.* Sensors, 2023. **23**(3): p. 1242.
48. ASTM C788-21, *Standard Specification for Standard Sand*. 2021, ASTM International: West Conshohocken, PA.
49. ASTM C1260-21, *Standard Test Method for Potential Alkali Reactivity of Aggregates (Mortar-Bar Method)*. 2021, ASTM International: West Conshohocken, PA.
50. ASTM C311-22, *Standard Test Methods for Sampling and Testing Fly Ash or Natural Pozzolans for Use as a Mineral Admixture in Portland-Cement Concrete*. 2022, ASTM International West Conshohocken, PA.
51. ASTM C1430-17, *Standard Test Method for Fineness of Hydraulic Cement by the 45-Mm (No. 325) Sieve*. 2017, ASTM International: West Conshohocken, PA.
52. ASTM C114-18, *Standard Test Methods for Chemical Analysis of Hydraulic Cement*. 2018, ASTM International,: West Conshohocken, PA.
53. ASTM C188-17, *Standard Test Method for Density of Hydraulic Cement*. 2017, ASTM International: West Conshohocken, PA.
54. Gražulis, S., Chateigner, D., Downs, R.T., Yokochi, A., Quirós, M., Lutterotti, L., Manakova, E., Butkus, J., Moeck, P., and Le Bail, A., *Crystallography Open Database–an Open-Access Collection of Crystal Structures.* Journal of applied crystallography, 2009. **42**(4): p. 726-729.
55. Gražulis, S., Merkys, A., and Vaitkus, A., *Crystallography Open Database (Cod).* Handbook of Materials Modeling: Methods: Theory and Modeling, 2020: p. 1863-1881.
56. Zeng, Q., Li, K., Fen-chong, T., and Dangla, P., *Determination of Cement Hydration and Pozzolanic Reaction Extents for Fly-Ash Cement Pastes.* Construction and Building Materials, 2012. **27**(1): p. 560-569.
57. Hanehara, S., Tomosawa, F., Kobayakawa, M., and Hwang, K., *Effects of Water/Powder Ratio, Mixing Ratio of Fly Ash, and Curing Temperature on Pozzolanic Reaction of Fly Ash in Cement Paste.* Cement and Concrete Research, 2001. **31**(1): p. 31-39.

58. Avet, F., Snellings, R., Diaz, A.A., Haha, M.B., and Scrivener, K., *Development of a New Rapid, Relevant and Reliable (R3) Test Method to Evaluate the Pozzolanic Reactivity of Calcined Kaolinitic Clays.* Cement and Concrete Research, 2016. **85**: p. 1-11.
59. Suraneni, P. and Weiss, J., *Examining the Pozzolanicity of Supplementary Cementitious Materials Using Isothermal Calorimetry and Thermogravimetric Analysis.* Cement and Concrete Composites, 2017. **83**: p. 273-278.
60. Snellings, R. and Scrivener, K.L., *Rapid Screening Tests for Supplementary Cementitious Materials: Past and Future.* Materials and Structures, 2016. **49**: p. 3265-3279.
61. Kim, T. and Olek, J., *Effects of Sample Preparation and Interpretation of Thermogravimetric Curves on Calcium Hydroxide in Hydrated Pastes and Mortars.* Transportation research record, 2012. **2290**(1): p. 10-18.
62. Holmes, N., Tyrer, M., West, R., Lowe, A., and Kelliher, D., *Using Phreeqc to Model Cement Hydration.* Construction and Building Materials, 2022. **319**: p. 126129.
63. Holmes, N., Kelliher, D., and Tyrer, M., *Thermodynamic Cement Hydration Modelling Using Hydcem*, in *CERI: Civil Engineering Research in Ireland (CERI)* 2020: Online.
64. Lothenbach, B., *Thermodynamic Equilibrium Calculations in Cementitious Systems.* Materials and Structures, 2010. **43**: p. 1413-1433.
65. Bharadwaj, K., Isgor, O.B., and Weiss, W.J., *A Simplified Approach to Determine Pozzolanic Reactivity of Commercial Supplementary Cementitious Materials.* Concrete International, 2022. **44**(1): p. 27-32.
66. Bharadwaj, K., Isgor, O.B., and Weiss, W.J., *A Dataset Containing Statistical Compositions and Reactivities of Commercial and Novel Supplementary Cementitious Materials; Dataset Version 1.0*. 2022: Oregon State University.
67. Bharadwaj, K., Isgor, O.B., and Weiss, W.J., *Pozzolanic Reactivity of Supplementary Cementitious Materials.* Materials Journal, 2023.
68. ASTM C109-20, *Standard Test Method for Compressive Strength of Hydraulic Cement Mortars (Using 2-In. Or [50-Mm] Cube Specimens)*. 2020, ASTM International: West Conshohocken, PA.
69. ASTM C1437-20, *Standard Test Method for Flow of Hydraulic Cement Mortar*. 2020, ASTM International: West Conshohocken, PA.
70. ASTM C1202-19, *Standard Test Method for Electrical Indication of Concrete's Ability to Resist Chloride Ion Penetration*. 2019, ASTM International: West Conshohocken, PA.
71. ASTM C1585-20, *Standard Test Method for Measurement of Rate of Absorption of Water by Hydraulic-Cement Concretes*. 2020, ASTM International: West Conshohocken, PA.
72. Kurda, R., de Brito, J., and Silvestre, J.D., *Water Absorption and Electrical Resistivity of Concrete with Recycled Concrete Aggregates and Fly Ash.* Cement and Concrete Composites, 2019. **95**: p. 169-182.
73. Mohebbi, M., Rajabipour, F., and Scheetz, B.E. *Reliability of Loss on Ignition (Loi) Test for Determining the Unburned Carbon Content in Fly Ash*. in *World of Coal Ash Conference (WOCA), Nashville, TN, May*. 2015.
74. Mohebbi, M., Rajabipour, F., and Scheetz, B.E., *Evaluation of Two-Atmosphere Thermogravimetric Analysis for Determining the Unburned Carbon Content in Fly Ash.* Advances in Civil Engineering Materials, 2017. **6**(1): p. 258-279.
75. Fan, M. and Brown, R.C., *Comparison of the Loss-on-Ignition and Thermogravimetric Analysis Techniques in Measuring Unburned Carbon in Coal Fly Ash.* Energy & fuels, 2001. **15**(6): p. 1414-1417.
76. Payá, J., Monzó, J., Borrachero, M., Perris, E., and Amahjour, F., *Thermogravimetric Methods for Determining Carbon Content in Fly Ashes.* Cement and concrete research, 1998. **28**(5): p. 675-686.
77. Scrivener, K., Snellings, R., and Lothenbach, B., *A Practical Guide to Microstructural Analysis of Cementitious Materials*. 2016: Taylor & Francis.

78. Sani, M.S.H.M., Muftah, F., and Muda, Z., *The Properties of Special Concrete Using Washed Bottom Ash (Wba) as Partial Sand Replacement.* International Journal of Sustainable Construction Engineering and Technology, 2010. **1**(2): p. 65-76.
79. Akın, S.Ş., Magalhaes, D., and Kazanc, F., *A Study on the Effects of Various Combustion Parameters on the Mineral Composition of Tunçbilek Fly Ash.* Fuel, 2020. **275**: p. 117881.
80. Ju, T., Meng, Y., Han, S., Lin, L., and Jiang, J., *On the State of the Art of Crystalline Structure Reconstruction of Coal Fly Ash: A Focus on Zeolites.* Chemosphere, 2021. **283**: p. 131010.
81. Kutchko, B.G. and Kim, A.G., *Fly Ash Characterization by Sem–Eds.* Fuel, 2006. **85**(17-18): p. 2537-2544.
82. Matsui, Y. and Wakabayashi, N., *Evaluation of Ash Melting Behavior in Pulverized Coal-Fired Furnace from Proportion of Amorphous Phase in Fly Ash.* Fuel, 2019. **257**: p. 116002.
83. Yan, K., Guo, Y., Ma, Z., Zhao, Z., and Cheng, F., *Quantitative Analysis of Crystalline and Amorphous Phases in Pulverized Coal Fly Ash Based on the Rietveld Method.* Journal of Non-Crystalline Solids, 2018. **483**: p. 37-42.
84. Zeyad, A.M., Johari, M.M., Tayeh, B.A., and Yusuf, M.O., *Efficiency of Treated and Untreated Palm Oil Fuel Ash as a Supplementary Binder on Engineering and Fluid Transport Properties of High-Strength Concrete.* Construction and building materials, 2016. **125**: p. 1066-1079.
85. Johari, M.M., Zeyad, A., Bunnori, N.M., and Ariffin, K., *Engineering and Transport Properties of High-Strength Green Concrete Containing High Volume of Ultrafine Palm Oil Fuel Ash.* Construction and Building Materials, 2012. **30**: p. 281-288.
86. Li, Y., Lin, H., and Wang, Z., *Quantitative Analysis of Fly Ash in Hardened Cement Paste.* Construction and Building Materials, 2017. **153**: p. 139-145.
87. Wang, X.-Y., *Effect of Fly Ash on Properties Evolution of Cement Based Materials.* Construction and Building Materials, 2014. **69**: p. 32-40.
88. Cui, Y., Wang, L., Liu, J., Liu, R., and Pang, B., *Impact of Particle Size of Fly Ash on the Early Compressive Strength of Concrete: Experimental Investigation and Modelling.* Construction and Building Materials, 2022. **323**: p. 126444.
89. Sun, Y., Xie, S., Wu, C., Cui, J., Chen, D., Guo, F., Jiang, Z., Ren, Y., and Lu, W., *Influence of the Ultra-Fine Fly Ash Dosages on the Mechanical Properties of the Sulfoaluminate Cement-Based High Water Backfilling Material.* Scientific Reports, 2023. **13**(1): p. 1564.
90. Layssi, H., Ghods, P., Alizadeh, A.R., and Salehi, M., *Electrical Resistivity of Concrete.* Concrete international, 2015. **37**(5): p. 41-46.
91. Azarsa, P. and Gupta, R., *Electrical Resistivity of Concrete for Durability Evaluation: A Review.* Advances in Materials Science and Engineering, 2017. **2017**.
92. Kasaniya, M., Thomas, M.D., and Moffatt, E.G., *Pozzolanic Reactivity of Natural Pozzolans, Ground Glasses and Coal Bottom Ashes and Implication of Their Incorporation on the Chloride Permeability of Concrete.* Cement and Concrete Research, 2021. **139**: p. 106259.
93. Li, Y.-X., Chen, Y.-M., Wei, J.-X., He, X.-Y., Zhang, H.-T., and Zhang, W.-S., *A Study on the Relationship between Porosity of the Cement Paste with Mineral Additives and Compressive Strength of Mortar Based on This Paste.* Cement and concrete research, 2006. **36**(9): p. 1740-1743.
94. Naik, T.R., Kumar, R., Ramme, B.W., and Kraus, R.N. *Effect of High-Carbon Fly Ash on the Electrical Resistivity of Fly Ash Concrete Containing Carbon Fibers*. in *Proceedings of the Conference on Sustainable Construction Materials and Technologies, Italy*. 2010.
95. Duchesne, J. and Bérubé, M., *The Effectiveness of Supplementary Cementing Materials in Suppressing Expansion Due to Asr: Another Look at the Reaction Mechanisms Part 2: Pore Solution Chemistry.* Cement and Concrete Research, 1994. **24**(2): p. 221-230.
96. Canham, I., Page, C., and Nixon, P., *Aspects of the Pore Solution Chemistry of Blended Cements Related to the Control of Alkali Silica Reaction.* Cement and Concrete Research, 1987. **17**(5): p. 839-844.

97. Pandey, S. and Sharma, R., *The Influence of Mineral Additives on the Strength and Porosity of Opc Mortar.* Cement and concrete research, 2000. **30**(1): p. 19-23.
98. Morris, W., Moreno, E., and Sagüés, A., *Practical Evaluation of Resistivity of Concrete in Test Cylinders Using a Wenner Array Probe.* Cement and concrete research, 1996. **26**(12): p. 1779-1787.
99. Horňáková, M. and Lehner, P., *Relationship of Surface and Bulk Resistivity in the Case of Mechanically Damaged Fibre Reinforced Red Ceramic Waste Aggregate Concrete.* Materials, 2020. **13**(23): p. 5501.
100. Ghosh, P. and Tran, Q., *Correlation between Bulk and Surface Resistivity of Concrete.* International Journal of Concrete Structures and Materials, 2015. **9**: p. 119-132.
101. Mousavinejad, S.H.G. and Sammak, M. *Strength and Chloride Ion Penetration Resistance of Ultra-High-Performance Fiber Reinforced Geopolymer Concrete*. in *Structures*. 2021. Elsevier.
102. Akhnoukh, A. *Overview of Concrete Durability Evaluation Using Electrical Resistivity*. in *Collaboration and Integration in Construction, Engineering, Management and Technology: Proceedings of the 11th International Conference on Construction in the 21st Century, London 2019*. 2021. Springer.
103. Rajabipour, F. and Weiss, J., *Electrical Conductivity of Drying Cement Paste.* Materials and Structures, 2007. **40**: p. 1143-1160.
104. Fanijo, E.O., Kolawole, J.T., and Almakrab, A., *Alkali-Silica Reaction (Asr) in Concrete Structures: Mechanisms, Effects and Evaluation Test Methods Adopted in the United States.* Case Studies in Construction Materials, 2021. **15**: p. e00563.
105. Saha, A.K., Khan, M.N.N., Sarker, P.K., Shaikh, F.A., and Pramanik, A., *The Asr Mechanism of Reactive Aggregates in Concrete and Its Mitigation by Fly Ash: A Critical Review.* Construction and Building Materials, 2018. **171**: p. 743-758.
106. Diamond, S., *Effects of Two Danish Flyashes on Alkali Contents of Pore Solutions of Cement-Flyash Pastes.* Cement and Concrete Research, 1981. **11**(3): p. 383-394.
107. Hobbs, D., *Influence of Pulverized–Fuel Ash and Granulated Blastfurnace Slag Upon Expansion Caused by the Alkali–Silica Reaction.* Magazine of concrete Research, 1982. **34**(119): p. 83-94.
108. Thomas, M., *The Effect of Supplementary Cementing Materials on Alkali-Silica Reaction: A Review.* Cement and concrete research, 2011. **41**(12): p. 1224-1231.
109. Rayment, P., *The Effect of Pulverised-Fuel Ash on the C/S Molar Ratio and Alkali Content of Calcium Silicate Hydrates in Cement.* Cement and Concrete Research, 1982. **12**(2): p. 133-140.
110. Monteiro, P., Wang, K., Sposito, G., Dos Santos, M., and de Andrade, W.P., *Influence of Mineral Admixtures on the Alkali-Aggregate Reaction.* Cement and concrete research, 1997. **27**(12): p. 1899-1909.
111. Hong, S.-Y. and Glasser, F.P., *Alkali Sorption by Csh and Cash Gels: Part Ii. Role of Alumina.* Cement and Concrete Research, 2002. **32**(7): p. 1101-1111.
112. Lothenbach, B., Scrivener, K., and Hooton, R., *Supplementary Cementitious Materials.* Cement and concrete research, 2011. **41**(12): p. 1244-1256.
113. Rajabipour, F., Sant, G., and Weiss, J., *Interactions between Shrinkage Reducing Admixtures (Sra) and Cement Paste's Pore Solution.* Cement and Concrete Research, 2008. **38**(5): p. 606-615.
114. Basheer, L., Kropp, J., and Cleland, D.J., *Assessment of the Durability of Concrete from Its Permeation Properties: A Review.* Construction and building materials, 2001. **15**(2-3): p. 93-103.
115. Zhuang, S., Wang, Q., and Zhang, M., *Water Absorption Behaviour of Concrete: Novel Experimental Findings and Model Characterization.* Journal of Building Engineering, 2022. **53**: p. 104602.
116. Claisse, P.A., Elsayad, H.I., and Shaaban, I.G., *Absorption and Sorptivity of Cover Concrete.* Journal of Materials in Civil Engineering, 1997. **9**(3): p. 105-110.
117. Moradllo, M.K., Qiao, C., Isgor, B., Reese, S., and Weiss, W.J., *Relating Formation Factor of Concrete to Water Absorption.* ACI Materials Journal, 2018. **115**(6): p. 887-898.

118. McCarthy, M., Robl, T., and Csetenyi, L., *Coal Combustion Products (Ccps): Characterization, Utilization and Beneficiation*. 2017, Elsevier Ltd.
119. Bartoňová, L., *Unburned Carbon from Coal Combustion Ash: An Overview.* Fuel Processing Technology, 2015. **134**: p. 136-158.
120. Straka, P., Náhunková, J., and Žaloudková, M., *Analysis of Unburned Carbon in Industrial Ashes from Biomass Combustion by Thermogravimetric Method Using Boudouard Reaction.* Thermochimica Acta, 2014. **575**: p. 188-194.
121. Brown, R.C. and Dykstra, J., *Systematic Errors in the Use of Loss-on-Ignition to Measure Unburned Carbon in Fly Ash.* Fuel, 1995. **74**(4): p. 570-574.
122. ASTM D6316, *Standard Test Method for Determination of Total, Combustible and Carbonate Carbon in Solid Residues from Coal and Coke*. 2017, ASTM International West Conshohocken, PA.
123. Harris, N.J., Hover, K.C., Folliard, K.J., and Ley, T., *Variables Affecting the Astm Standard C 311 Loss on Ignition Test for Fly Ash.* Journal of ASTM International, 2006. **3**(8): p. JAI100286.
124. Zhu, H., Li, C., Cheng, Y., Jiang, Z., and Wu, K., *Pozzolanicity of Fly Ash Modified by Fluidized Bed Reactor–Vapor Deposition.* Construction and Building Materials, 2017. **156**: p. 719-727.
125. Yazici, Ş. and Arel, H.Ş., *Effects of Fly Ash Fineness on the Mechanical Properties of Concrete.* Sadhana, 2012. **37**(3): p. 389-403.
126. Chindaprasirt, P., Jaturapitakkul, C., and Sinsiri, T., *Effect of Fly Ash Fineness on Compressive Strength and Pore Size of Blended Cement Paste.* Cement and concrete composites, 2005. **27**(4): p. 425-428.
127. Moghaddam, F., Sirivivatnanon, V., and Vessalas, K., *The Effect of Fly Ash Fineness on Heat of Hydration, Microstructure, Flow and Compressive Strength of Blended Cement Pastes.* Case Studies in Construction Materials, 2019. **10**: p. e00218.
128. Chindaprasirt, P., Homwuttiwong, S., and Sirivivatnanon, V., *Influence of Fly Ash Fineness on Strength, Drying Shrinkage and Sulfate Resistance of Blended Cement Mortar.* Cement and Concrete Research, 2004. **34**(7): p. 1087-1092.
129. Sinsiri, T., Chindaprasirt, P., and Jaturapitakkul, C., *Influence of Fly Ash Fineness and Shape on the Porosity and Permeability of Blended Cement Pastes.* International Journal of Minerals, Metallurgy, and Materials, 2010. **17**(6): p. 683-690.
130. Chindaprasirt, P., Jaturapitakkul, C., and Sinsiri, T., *Effect of Fly Ash Fineness on Microstructure of Blended Cement Paste.* Construction and Building Materials, 2007. **21**(7): p. 1534-1541.
131. Wang, Y., Burris, L.E., Shearer, C.R., Hooton, R.D., and Suraneni, P., *Characterization and Reactivity of Size-Fractionated Unconventional Fly Ashes.* Materials and structures, 2023. **56**(3): p. 49.
132. Ramanathan, S., Kasaniya, M., Tuen, M., Thomas, M.D., and Suraneni, P., *Linking Reactivity Test Outputs to Properties of Cementitious Pastes Made with Supplementary Cementitious Materials.* Cement and Concrete Composites, 2020. **114**: p. 103742.
133. Kasaniya, M., Thomas, M.D., and Moffatt, E.G., *Development of Rapid and Reliable Pozzolanic Reactivity Test Method.* ACI Materials Journal, 2019. **116**(4): p. 145-154.
134. Suraneni, P., Hajibabaee, A., Ramanathan, S., Wang, Y., and Weiss, J., *New Insights from Reactivity Testing of Supplementary Cementitious Materials.* Cement and Concrete Composites, 2019. **103**: p. 331-338.
135. Ramanathan, S., Moon, H., Croly, M., Chung, C.-W., and Suraneni, P., *Predicting the Degree of Reaction of Supplementary Cementitious Materials in Cementitious Pastes Using a Pozzolanic Test.* Construction and Building Materials, 2019. **204**: p. 621-630.
136. Durdziński, P.T., Ben Haha, M., Bernal, S.A., De Belie, N., Gruyaert, E., Lothenbach, B., Menéndez Méndez, E., Provis, J.L., Schöler, A., and Stabler, C., *Outcomes of the Rilem Round Robin on Degree of Reaction of Slag and Fly Ash in Blended Cements.* Materials and Structures, 2017. **50**: p. 1-15.